

POST-EQUINOX DYNAMICS AND POLAR CLOUD STRUCTURE ON URANUS[†]

L. A. SROMOVSKY¹, P. M. FRY¹, H. B. HAMMEL^{2,3}, I. DE PATER⁴, AND K. A. RAGES⁵

Journal reference: Icarus 220 (2012) 694-712.

ABSTRACT

Post equinox imaging of Uranus by HST, Keck, and Gemini telescopes has enabled new measurements of winds over previously sampled latitudes as well as measurements at high northern latitudes that have recently come into better view. These new observations also used techniques to greatly improve signal to noise ratios, making possible the detection and tracking of more subtle cloud features. The 250 m/s prograde jet peaking near 60°N was confirmed and more accurately characterized. Several long-lived cloud features have also been tracked. The winds pole-ward of 60°N are consistent with solid body rotation at a westward (prograde) rate of 4.3°/h with respect to Uranus' interior. When combined with 2007 and other recent measurements, it is clear that a small but well-resolved asymmetry exists in the zonal profile at middle latitudes, peaking at 35°, where southern winds are 20 m/s more westward than corresponding northern winds. High S/N Keck II imaging of the north polar region of Uranus reveals a transition from streaky bands below 60° N to a region from 60° to nearly the north pole, where widely distributed small bright spots, resembling cumulus cloud fields, with several isolated dark spots, are the dominant style of cloud features. This presents a stark contrast to 2003 detailed views of the south polar region of Uranus when no discrete cloud features could be detected in comparable Keck II near-IR images. The pressure levels of discrete clouds estimated from spatial modulations in H and Hcont images indicate that the polar cloud features are generally in the 1.3 to 2-3 bar range, as are equatorial and several mid-latitude features. Several of the brighter mid latitude features are found above the 1.2-bar level of methane condensation.

Subject headings: Uranus, Uranus Atmosphere; Atmospheres, dynamics

1. INTRODUCTION

The last update to the wind profile of Uranus was assembled by Sromovsky et al. (2009) from intensive observations carried out near the time of the 2007 equinox of Uranus. These results were compared with past results from 1986 Voyager observations (Smith et al. 1986), 1997 NICMOS observations (Karkoschka 1998), 1997-2000 HST observations (Hammel et al. 2001), a remeasurement of 2003 Keck results (Hammel et al. 2005; Sromovsky et al. 2009), Keck results from 2003 and 2004 (Sromovsky and Fry 2005), 2005 Keck results (Sromovsky et al. 2007), and 2006 Keck results (Hammel et al. 2009). Taken together, these data sets provided evidence for a small asymmetry in the zonal wind profile, but no substantial evidence for any systematic long-term temporal variation that might be associated with seasonal variations. The 2007 observations finally were able to detect cloud features up to 70°N, and obtained precise wind measurements up to 62°N (planetocentric) latitude, for the first time showing the beginnings of a northern prograde jet peak with a speed near 250 m/s.

Since 2007 the north polar region of Uranus has become

much better exposed to view as the sub-solar latitude has moved to 14°N during the 2011 opposition. This gave us a chance to better determine the zonal wind profile in the northern hemisphere and provide a much better characterization of the prograde jet. In the following we describe the post equinox observations that we used to better define the circulation of Uranus, the measurement results from each data set, new views of the north polar region of Uranus and the different styles of discrete cloud features located there, and finally we describe altitude constraints on a subset of these features.

2. OBSERVATIONS

The observations were made with four cameras on three observatories. The camera characteristics for each observing configuration are given in Table 1, and the imaging observations of Uranus acquired between 2009 and 2011 are listed in Table 2. The SNAP observations, acquired in October 2009 and July and August 2010, do not provide temporal sampling adequate to measure wind speeds within each SNAP data set. However, they can provide useful constraints on the motions of long lived features when combined with other observations. The November 2009 HST observations do provide temporal sampling adequate to obtain precise wind measurements, although the number of cloud targets contained in these images is small because of limited spatial resolution and inherently low contrast of cloud features at the observed wavelengths. (Longer wavelengths of higher contrast were not used because the required WFC3 IR camera has a much coarser pixel scale of 0.13 arcseconds/pixel.) The HST imaging program was designed to achieve high S/N ratios to compensate for the inherently low contrast of the images, which made it possible to ob-

¹ University of Wisconsin - Madison, Madison WI 53706

² AURA, 1212 New York Ave. NW, Suite 450, Washington, DC 20005, USA

³ Space Science Institute, Boulder, CO 80303, USA

⁴ University of California, Berkeley, CA 94720, USA

⁵ SETI Institute, Mountain View, CA 94043, USA

[†] Based in part on observations with the NASA/ESA Hubble Space Telescope obtained at the Space Telescope Science Institute, which is operated by the Association of Universities for Research in Astronomy, Incorporated under NASA Contract NAS5-26555.

TABLE 1
TELESCOPE/CAMERA CHARACTERISTICS.

Telescope	Mirror Diam.	Camera	Pixel size	Diff Lim @ Wavelength
HST	2.3 m	WFC3	0.04''	0.09'' @ 0.85 μm
Gemini-North	8 m	NIRI	0.0218''	0.05'' @ 1.6 μm
Keck II	10 m	NIRC2-NA	0.00994''	0.04'' @ 1.6 μm
Keck II	10 m	NIRC2-WA	0.039686''	0.04'' @ 1.6 μm

NOTES: Both groundbased telescopes have adaptive optics capability, but only Keck II can use Uranus itself as the wave front reference. Our Gemini observations had to use a satellite of Uranus for the wave front reference.

tain 6 wind vectors with an accuracy of 3-12 m/s, and one with an accuracy of 33 m/s (Fry et al. 2012). The 3 and 4 June 2010 HST observations provide complete longitude coverage, but detected only a single discrete cloud feature near 29° N, and did not provide temporal sampling adequate to determine an accurate wind vector. The July and August 2010 observations also each provide only a small temporal span and thus can only be used to track long-lived features if any are observed. There are two relatively prominent features and one faint feature in the July 17 images and also three similar features at similar latitudes in the 5 August images. However, it is unclear if these are the same features.

In Table 1, the pixel scale of 0.2138 ± 0.0005 arcsec/pixel listed for the Gemini NIRI camera was derived by us from measurements of Uranus and its satellites in comparison with HORIZON ephemeris positions. This scale applies when the field lens is used and differs by 2% from the standard pixel scale of 0.219 arcseconds/pixel given by the NIRI instrument web page or the value of 0.218 arcseconds/pixel listed under the file header PIXSCALE keyword, which is only valid without the field lens. We were motivated to measure the pixel scale by observed deviations from uniform motion as cloud targets approached the limb of the planet. That problem went away after the pixel scale was revised. The penetration of these filters into a clear Uranus atmosphere are shown in Fig. 1.

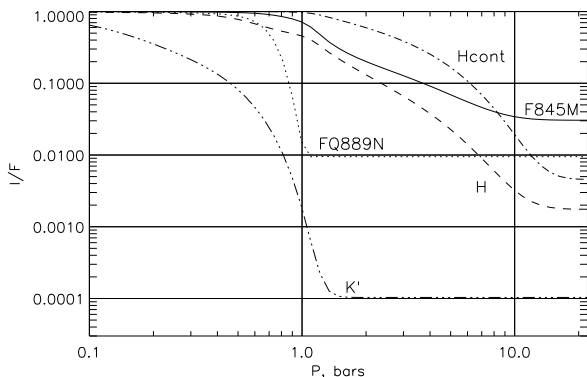


FIG. 1.— I/F for a unit-albedo surface in a clear Uranian atmosphere as a function of the pressure at which the surface is placed. This shows how much cloud reflectivity in each filter is attenuated by atmospheric absorption above the cloud. The high pressure limits correspond to the reflectivity of a clear atmosphere.

3. IMAGE PROCESSING AND NAVIGATION

Most of our post equinox observations are derived from data sets designed to provide high S/N images. The potential of this approach, and results obtained from 2009 HST WFC3 imaging, are described by Fry et al. (2012). Briefly, the approach is to take exposures short enough to avoid significant smear due to planetary rotation during the exposure, then average eight or more exposures together on a latitude-longitude grid to remove the effects of planetary rotation. Near the limb of the planet, images with better views are given greater weight: we required the view angle cosine to be greater than 0.025 and weighted each point by the square of the cosine. This averaging process allows the detection of more subtle cloud features than would otherwise be possible. Sample results are illustrated in Fig. 2, where a single H image (A) is compared with an 8-image average (B, C). Little difference is seen in the direct images because the latitudinal variations in brightness are far greater than the noise levels in both images. But when the large-scale latitudinal variations are removed by subtracting a $15\text{-pixel} \times 15\text{-pixel}$ boxcar smoothed version of each image, the improved S/N level of the averaged image becomes quite obvious, as well as the improved visibility of subtle details in the cloud structure. The measured central-disk noise level of the single image is about 0.44% of signal, and improves to about 0.17% in the 8-image average. This improvement is about a factor of 2.6, which is slightly below the factor of 2.83 ($\sqrt{8}$) expected for completely random noise.

Except for the image S/N enhancement described above and in more detail by Fry et al. (2012), image processing and navigation followed the same procedures described by Sromovsky et al. (2009). We used standard 1-bar polar and equatorial radii of 24,973 km and 25,559 km respectively, and a longitude system based on a 17.24-hour rotation period (Seidemann et al. 2002).

4. CLOUD TRACKING

4.1. Methodology

Initially, wind vectors were obtained via manual tracking of discrete cloud features in high-pass filtered images, following the same general approach described by Sromovsky et al. (2009). Measurements of longitude and latitude vs. time were fit to straight lines using both unweighted regressions. We used the weighted fit for the wind estimate and the larger of weighted and unweighted error estimates for the assigned error. Errors in latitude and longitude were initially computed assuming an angular error of 0.6 image pixels, based on Sromovsky et al. (2009). These estimated errors vary with view angle and position on the disk, and are important when the number

TABLE 2
 IMAGING OBSERVATIONS USED TO TRACK DISCRETE CLOUD FEATURES.

Date	Time Range	Telescope/Program	PI	Filters (images)
13 Oct. 2009	4:36-4:54	HST/SNAP 11630	KAR	F845M (12)
11 Nov. 2009	13:16-22:00	HST/11573	LAS	F845M (48)
12 Nov. 2009	13:14-13:59	HST/11573	LAS	F845M (48)
3 June 2009	9:44-15:14	HST/11573	LAS	F467M, F658N(2), FQ727N, FQ750N, FQ937N(2), FQ889N(2), FQ906N(2), FQ924N(2), FQ619N, F547M, F763M, F845M
4 June 2009	14:30-15:12	HST/11573	LAS	FQ619N, F547M, F658N, F763M, F845M, FQ924N, FQ906N, FQ889N, FQ937N
17 July 2010	3:55-4:12	HST/SNAP 11630	KAR	F845M (12)
5 Aug. 2010	1:48-2:54	HST/SNAP 11630	KAR	F845M (12)
2 Nov. 2010		Gemini-N/2010B-Q-110	LAS	J(4), H(4), K'(8), Hcont(4), CH4L(4)
3 Nov. 2010		Gemini-N/2010B-Q-110	LAS	J(4), H(4), K'(8), Hcont(4), CH4L(4)
26 July 2011	10:51-15:51	Keck/NIRC2 N128N2	LAS	H(87), Hcont(19), K', CH4.long
27 July 2011	14:02-14:09	Keck/NIRC2 N128N2	LAS	H(4), Hcont(3)
28 July 2011	10:51-15:32	Keck/NIRC2 N128N2	IDP	H(30), K'(7)
23 Oct. 2011	5:34-6:29	Gemini-N/2011B-Q-105	LAS	H(10), Hcont(10)
25 Oct. 2011	5:48-9:01	Gemini-N/2011B-Q-105	LAS	H(11), Hcont(19)
26 Oct. 2011	5:05-8:58	Gemini-N/2011B-Q-105	LAS	H(40), Hcont(72)

NOTE: Times are UTC. The numbers in the HST filter names correspond to their central wavelengths in nanometers. Many of the listed images need to be combined to obtain adequate S/N ratios.

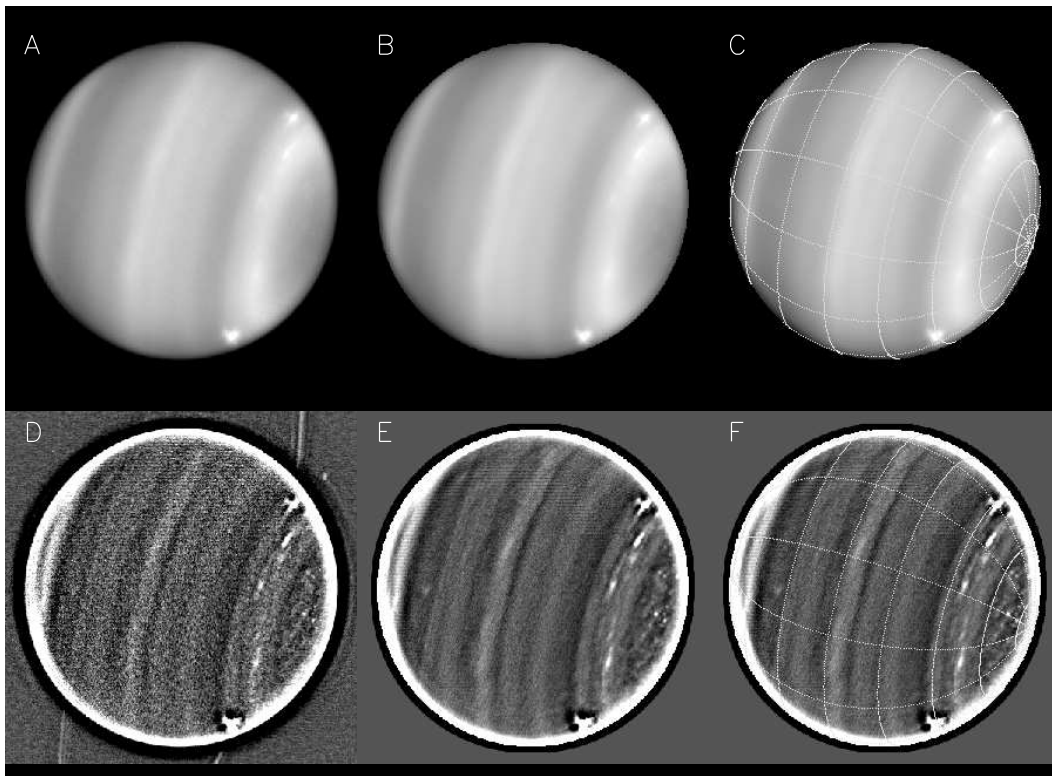


FIG. 2.— Keck II NIRC2 H-filter image (2-minute exposure) from 26 July 2011 (A) compared to an 8-image average with planet rotation removed (B). High-pass filtered versions (D) and (E), obtained by subtracting a 15-pixel \times 15-pixel boxcar smoothed version from each, reveal a 2.6:1 improvement in S/N ratio. The latitude grids in C and F are at 20° intervals starting at the equator. The longitude grids are at 30° intervals.

of target measurements is small. But when the number of samples is large, the RMS deviation of the measurements from a straight line fit is a better measure of the

errors, as it includes both navigation errors as well as target measurement errors. We find that tracking errors are generally larger in longitude than in latitude

because cloud brightness gradients are generally much larger along meridians than along lines of constant latitude. The main exceptions to this rule are the small symmetrical spots seen in the north polar region of Uranus.

We also made extensive use of maximum correlation tracking to try to increase the number of cloud targets and to reduce the errors in defining their positions. To implement this approach we displayed an image sequence as a stacked series of narrow horizontal strips, each containing an orthogonal projection covering a specified range of longitudes and a narrow range of latitudes. For each cloud target visible in the selected latitude range, a reference image is selected and a target box is adjusted in size and position so that it contains the cloud feature and a small region outside of it. Target boxes in other images are initially positioned using the 2007 wind measurements, then manually adjusted in images in which the default position fails to contain the target feature. The positions of the target boxes in all but the reference image are then automatically refined to maximize the cross correlation between the reference target box signal variations and those contained in each of the other boxes. To reduce the impact of large-scale variations such as produced by latitude bands, we use high-pass filters or median image subtraction. The correlation tracking usually takes a few iterations to achieve convergence. This procedure facilitated the identification of more cloud targets, as well as providing generally more accurate tracking results than purely manual measurements. For compact bright features of relatively high contrast we also found it sometimes useful for cloud tracking to use the center-of-differential brightness coordinates x_{CDB} and y_{CDB} , which are given by the sums

$$x_{CDB} = \sum_{i,j}^{target} x_i \cdot [I(i,j) - I_B(i,j)] / \quad (1)$$

$$y_{CDB} = \sum_{i,j}^{target} y_j \cdot [I(i,j) - I_B(i,j)] / \quad (2)$$

$$\sum_{i,j}^{target} [I(i,j) - I_B(i,j)]$$

where $I(i,j)$ is the reflectivity at image location i,j , $I_B(i,j)$ is either the smoothed reflectivity or the median filtered image reflectivity, and the summation is over the area of the target box. What we see in the filtered or subtracted images is $I - I_B$ rather than I .

4.2. July 2011 Keck results

In our July 2011 Keck NIRC2 images we were able to identify 21 targets suitable for tracking the winds of Uranus. Most of these were only trackable within a single transit on 26 July 2011, when weather and seeing conditions did not severely impact the NIRC2 images. On the 27th, turbulence increased significantly during the second half of the night, when our observations were taken, and seeing reached extremely poor levels up to several arc seconds FWHM, at which point the AO system im-

age quality deteriorates drastically. Poor seeing was also the rule on 28 July, although it was highly variable and a few usable images were obtained. But it was only the 26 July images that could be combined together to produce enhanced signal-to-noise ratios, which facilitated tracking of small low-contrast cloud features.

Even the 26 July images were far below the excellent quality frequently obtained in prior observations, and thus it was not surprising that the expected bounty of low contrast features implied by the proof-of-concept image of Fry et al. (2012) did not materialize. Not only was seeing below par (rapidly varying from $0.6''$ to $1.2''$ and beyond), but PSF characteristics (unusual wing structure not normally visible) suggested that the AO system might have been out of adjustment as well (this was later confirmed during the November observing run of de Pater and Hammel). Nevertheless, our imaging program design partially compensated for these problems. We were able to make a significant improvement in the definition of the northern hemisphere prograde jet, as illustrated in Fig. 3. The wind accuracy we obtained for targets we could track was quite impressive, often reaching uncertainties below 10 m/s. These new manual tracking results are roughly consistent with the 10-term Legendre polynomial fit of Sromovsky et al. (2009), which is based on wind measurements acquired during the intensive observing period near the 2007 equinox. We also obtained excellent views of high northern latitudes that we present in a later section.

We reanalyzed the Keck data set using the stacked remapped strips and manually assisted cross-correlation method. This enabled us to identify 40 cloud targets in the 26 July data set alone. Because only the prominent cloud features can be reliably identified after more than one planet rotation, we did not attempt to use these correlation-based techniques on multiple days simultaneously. For such features our manual tracking already provides very high accuracy. The results from the maximum-correlation tracking are displayed in Fig. 4 and Table 4. The most accurate of the high latitude observations are shown in Fig. 4B. These are filtered to have low formal error estimates, high median correlation, and long tracking intervals. (Each cloud target has a reference box containing the target in one image that serves as a reference; the median correlation is the median of the cross-correlation maximum values between the reference and the subimage boxes in the other images.) These results highlight small but significant deviations from the Sromovsky et al. (2009) 10-term Legendre polynomial fit. In the north polar region in particular the polynomial fit has the wind speed and the longitudinal drift rate both approach zero towards the pole, while our new measurements suggests that the polar region is moving with solid body rotation at a drift rate near $4.3^\circ/\text{h}$ westward (the longitudinal drift rate is independent of latitude for solid-body rotation).

4.3. Gemini October 2011 results

Gemini-North observations were obtained during 23, 25, and 26 October 2011 (Table 2), with most of the high-quality imaging obtained during 26 October. As with the Keck II imaging in July, we used a program of repeated short exposures and averaging on latitude-longitude grids to improve S/N dramatically and eliminate smear due to

TABLE 3
 KECK II NIRC2 WIND RESULTS FROM 26-28 JULY 2011.

PC Lat. (°)	PG Lat. (°)	Longitude (° east)	MJDavg -55000	Drift rate (°/h east)	Zonal wind (m/s west)	ID	N	Δt (h)
77.07	77.64 ± 0.08	-4.7 ± 0.5	55768.5311	-4.25 ± 0.56	115.2 ± 15.4	1	13	3.02
73.81	74.51 ± 0.11	81.9 ± 0.3	55768.5758	-4.61 ± 0.35	155.8 ± 12.0	3	10	2.65
73.24	73.96 ± 0.17	313.6 ± 0.7	55770.5681	-4.34 ± 0.42	151.9 ± 14.9	10	3	3.98
70.65	71.46 ± 0.12	120.5 ± 0.5	55768.6065	-5.68 ± 0.76	228.6 ± 31.2	11	5	1.83
70.55	71.36 ± 0.12	106.4 ± 0.4	55768.5973	-4.03 ± 0.51	163.0 ± 20.9	12	6	2.24
69.85	70.70 ± 0.10	-5.0 ± 0.3	55768.5263	-4.04 ± 0.31	168.9 ± 13.4	2	9	3.02
67.14	68.08 ± 0.11	88.9 ± 0.3	55768.5883	-4.52 ± 0.30	213.4 ± 14.4	9	7	2.65
66.14	67.11 ± 0.03	97.0 ± 0.3	55768.6186	-4.23 ± 0.56	208.0 ± 27.7	6	5	1.41
62.99	64.05 ± 0.11	69.4 ± 0.2	55768.5975	-4.03 ± 0.26	222.4 ± 14.8	8	6	2.24
62.87	63.93 ± 0.11	78.3 ± 0.2	55768.5746	-4.64 ± 0.25	257.5 ± 13.8	7	9	3.06
50.91	52.20 ± 0.05	32.3 ± 0.1	55768.5526	-3.33 ± 0.16	256.5 ± 12.2	18	11	4.41
49.71	51.02 ± 0.05	17.5 ± 0.2	55768.5398	-3.23 ± 0.26	255.4 ± 20.9	24	7	4.02
47.09	48.41 ± 0.08	321.9 ± 0.2	55768.5077	-2.65 ± 0.31	220.8 ± 26.0	20	6	2.17
44.92	46.25 ± 0.07	-6.8 ± 0.1	55768.5252	-1.99 ± 0.12	172.7 ± 10.2	5	16	3.44
43.45	44.78 ± 0.04	124.5 ± 0.2	55768.6065	-2.35 ± 0.38	209.1 ± 33.4	19	5	1.83
40.86	42.18 ± 0.08	269.2 ± 0.2	55769.2099	-1.73 ± 0.01	160.9 ± 0.9	16	7	48.19
38.97	40.27 ± 0.07	72.0 ± 0.1	55768.7261	-1.41 ± 0.01	134.5 ± 0.9	13	12	52.17
29.17	30.31 ± 0.15	198.7 ± 0.5	55770.1698	-0.59 ± 0.04	63.7 ± 3.7	15	3	21.18
25.75	26.81 ± 0.07	128.8 ± 0.1	55768.7605	-0.08 ± 0.03	9.4 ± 2.9	14	7	24.01
-24.16	-25.16 ± 0.09	19.4 ± 0.1	55768.5252	-0.38 ± 0.09	42.5 ± 10.5	22	8	3.01
-40.37	-41.69 ± 0.15	29.0 ± 0.1	55768.5315	-1.33 ± 0.16	124.1 ± 14.8	23	6	2.50

NOTES: PC Lat. and PG Lat. are planetocentric and planetographic latitudes respectively. MJDavg denotes Modified Julian Date average for the N measurements used to determine the cloud motion, where $MJD = \text{Julian Date} - 2\,400\,000.5$. Δt is the time difference between the earliest and latest image used to track a given target.

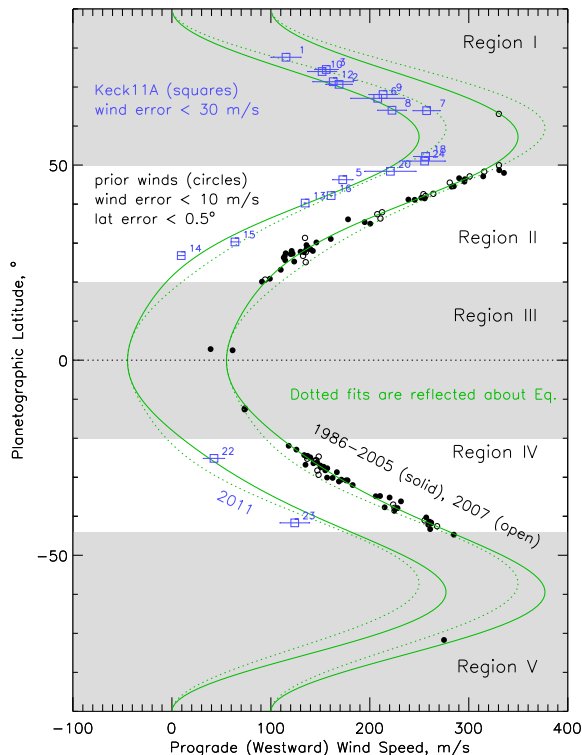


FIG. 3.— Keck II wind measurements from July 26-28 2011 (squares) with errors less than 30 m/s, compared to the 10-term Legendre polynomial fit of Sromovsky et al. (2009) (solid curves) and its inverse about the equator (dotted curves). Prior results are shown offset 100 m/s to the right. Numeric labels refer to cloud target IDs given in Table 3. Shaded regions (I, III, and V) are those poorly sampled by prior observations.

planet rotation. Sample improvements can be seen in Fig. 5, which compares single H and Hcont images with 8-image average versions.

Using a time-sequence display in combination with manual selection and tracking, we were able to track 21 cloud features; but only two were tracked long enough to determine highly accurate wind speeds. To improve our analysis of this data set we applied our stacked strip and cross-correlation tracking method. This led to an increase in the number of trackable features from 21 to 26, with 9 features tracked over more than a single transit, compared to just two in the initial manual effort. These long time spans yield extremely accurate drift rates and wind speeds, with uncertainties of less than $0.04^\circ/\text{h}$ and 4 m/s respectively. The results are listed in Table 5 and a subset are plotted in Fig. 6, where the wind results are compared to the 10-term Legendre fit of Sromovsky et al. (2009) and with the results of Fry et al. (2012), which are shown as filled squares. The latter results are in best agreement with the inverted Legendre fit, as is the most accurate of our Gemini wind measurements. Although this weakly suggests that the circulation may be in the process of seasonal change in the direction of reversing the north-south asymmetry observed during the last (2007) equinox, the number of samples supporting this change is too small to consider statistically significant. Most of the Gemini results are at latitudes where we already have significant numbers of samples, but Gemini and the Fry et al. (2012) results both contribute vectors in Region III, which has been grossly undersampled in most observations, due to a lack of cloud features visible at the available S/N.

4.4. Equatorial winds and cloud patterns

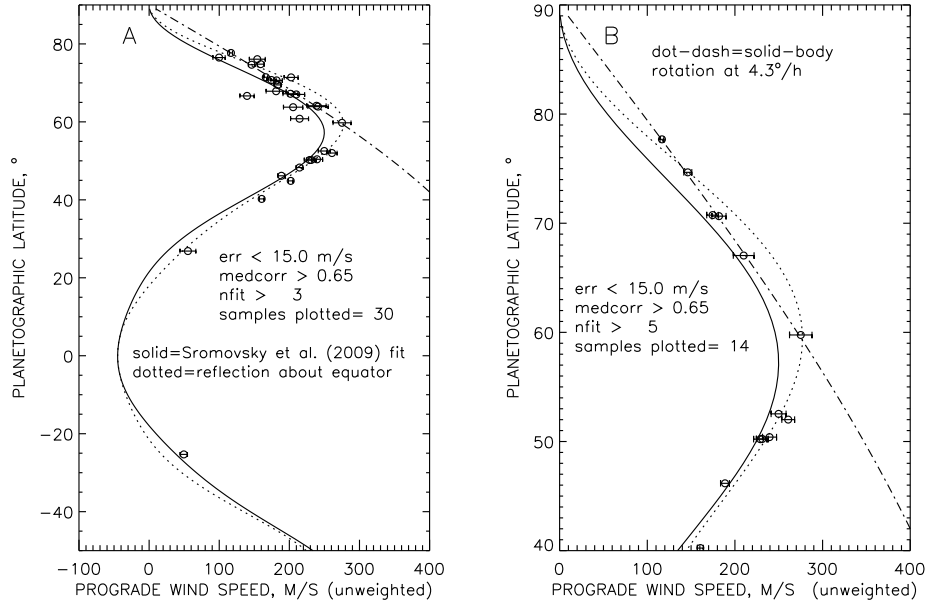


FIG. 4.— Winds obtained from automated (mainly maximum-correlation) cloud tracking in 26 July 2011 Keck imagery for all latitudes and the best 30 vectors (A), and for high latitudes and the best 14 vectors (B). The dot-dashed line in each figure indicates solid-body rotation (latitudinally invariant rate of change of longitude with time) at a rate of $4.3^\circ/\text{h}$ westward. In the legend *err* denotes wind speed error, *nfit* is the number of points defining the motion of a given cloud target, and *medcorr* is the median correlation coefficient between the reference cloud target box and all the other target boxes at their optimum displacements relative to the reference.

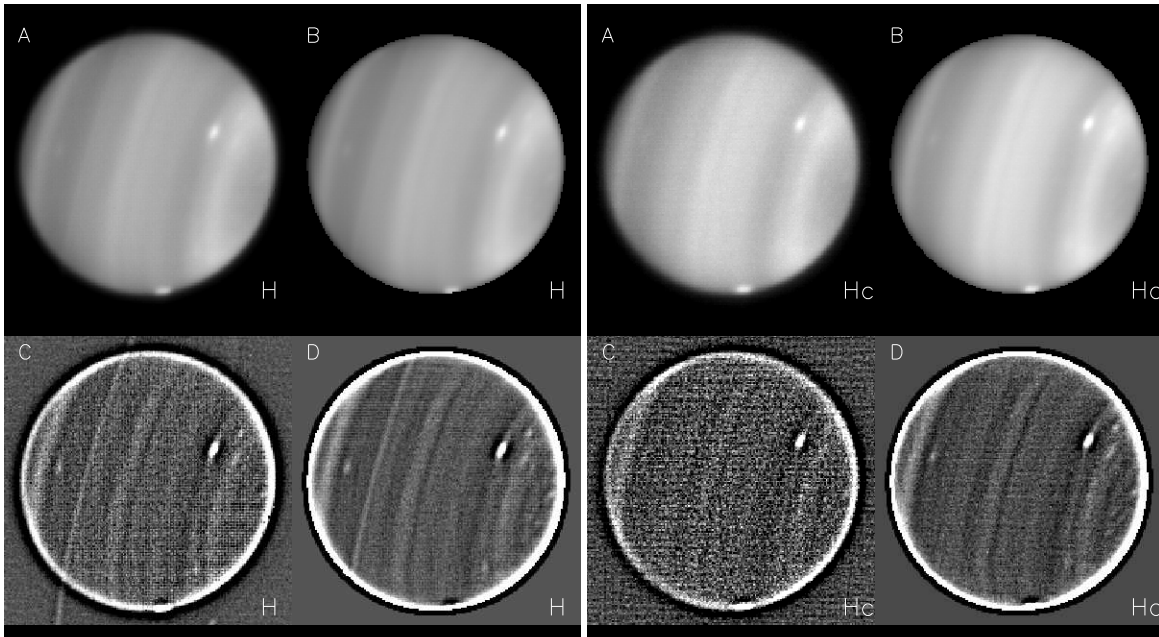


FIG. 5.— Left: Gemini-North H filter image from 26 October 2011 (A) compared to an 8-image average with planet rotation removed (B). All individual images were taken with a 2-minute exposure. High-pass filtered versions (C) and (D), obtained by subtracting a 7-pixel \times 7-pixel boxcar smoothed version from each, reveal a large improvement in S/N ratio. Right: Same as at left, except for the Hcont filter.

There are broad and fuzzy cloud patterns centered at approximately 4° N, which have a latitudinal width of $5\text{--}6^\circ$, a longitudinal extent of $\sim 8^\circ$, and a spacing of approximately 40° , which corresponds to a wavenumber-9 pattern of broad cloud features. A similar but more complete pattern was captured by 2003 Keck imagery, although in that case a wavenumber of 12 was inferred by Hammel et al. (2005). Given some variability in locating these broad features, it is not clear whether these

two patterns are really different. The 2011 equatorial features are most easily seen in images that have had a median image subtracted. A stack of remapped difference images of that type are shown in Fig. 7. Median subtraction has the effect of removing the zonally symmetric and latitude dependent background I/F variation, leaving only the additional brightness produced by the discrete cloud features. This is most effective when the images in the data set all have the same resolution and

TABLE 4
CORRELATION TRACKING RESULTS FROM 26 JULY 2011 KECK II IMAGES.

PC Lat. (°)	PG Lat. (°)	Longitude (° east)	MJDavg -55000	Drift rate (°/h east)	Zonal wind (m/s west)	ID	N	Δt (h)
77.67	78.21±0.25	122.3±0.3	768.6211	-3.51±0.44	90.9±11.3	706	3	1.41
77.12	77.69±0.15	-6.2±0.3	768.5352	-4.32±0.13	116.7±3.4	701	8	4.04
76.07	76.68±0.36	-36.6±0.8	768.4883	-5.48±0.92	159.9±26.8	707	4	1.37
75.88	76.50±0.29	5.5±0.5	768.5039	-3.37±0.30	99.7±8.7	702	5	2.60
75.45	76.08±0.13	-12.3±0.3	768.4883	-5.12±0.47	155.9±14.3	703	4	1.37
74.12	74.81±0.13	83.4±0.3	768.5938	-4.79±0.15	159.1±5.1	705	5	2.65
73.97	74.66±0.17	25.6±0.6	768.5469	-4.37±0.14	146.2±4.6	704	9	4.43
70.64	71.46±0.13	110.9±0.1	768.5938	-4.20±0.13	168.8±5.1	714	5	2.65
70.60	71.42±0.00	126.7±0.3	768.6055	-5.02±0.25	202.5±9.9	715	4	1.83
69.90	70.74±0.16	-7.0±0.4	768.5195	-4.18±0.16	174.5±6.6	708	7	3.02
69.80	70.65±0.24	43.2±0.6	768.5703	-4.34±0.19	181.8±8.1	719	6	3.49
68.60	69.49±0.07	4.4±0.3	768.5234	-4.14±0.12	183.4±5.1	709	5	3.02
66.92	67.86±0.22	91.5±0.6	768.5938	-3.80±0.30	181.1±14.3	713	5	2.65
66.37	67.33±0.25	77.8±0.6	768.5625	-4.65±0.18	226.6±8.9	720	7	3.91
66.24	67.20±0.18	103.7±0.5	768.5898	-4.12±0.22	201.5±10.6	740	5	3.06
66.07	67.04±0.20	16.2±0.4	768.5117	-4.26±0.24	210.0±11.8	710	6	2.60
65.68	66.66±0.10	-44.7±0.2	768.4883	-2.84±0.36	142.1±18.2	711	4	1.37
64.35	65.37±0.17	44.6±0.4	768.6055	-3.74±0.31	197.0±16.6	718	4	1.83
63.08	64.14±0.13	73.7±0.3	768.6055	-4.33±0.25	238.7±13.7	716	4	1.83
62.85	63.91±0.13	80.1±0.3	768.6055	-4.34±0.26	240.9±14.4	717	4	1.83
62.70	63.77±0.18	-42.2±0.2	768.4883	-3.67±0.35	205.0±19.3	712	4	1.37
59.83	60.97±0.27	10.7±0.5	768.5117	-3.92±0.28	239.8±16.9	722	6	2.60
59.66	60.81±0.25	-10.4±0.2	768.5000	-3.49±0.21	214.6±12.8	721	5	1.78
58.59	59.76±0.20	63.4±0.7	768.5352	-4.33±0.20	275.1±12.8	723	8	4.04
51.63	52.92±0.06	126.4±0.3	768.6211	-4.01±0.41	304.3±30.9	734	3	1.41
51.30	52.59±0.20	135.9±0.2	768.6211	-3.25±0.27	248.1±20.9	733	3	1.41
51.24	52.53±0.31	25.4±0.5	768.5469	-3.27±0.11	249.8±8.5	728	9	4.43
50.71	52.01±0.21	30.2±0.3	768.5352	-3.37±0.09	260.8±7.3	724	8	4.04
49.09	50.40±0.54	56.3±0.3	768.5547	-2.99±0.10	239.5±8.0	727	7	3.91
48.92	50.23±0.19	45.6±0.3	768.5469	-2.88±0.09	231.3±6.8	725	9	4.43
48.90	50.21±0.24	-29.2±0.2	768.5117	-2.87±0.13	230.9±10.7	730	6	2.60
48.67	49.98±0.28	63.5±0.4	768.5625	-2.82±0.13	228.1±10.6	726	7	3.91
46.96	48.28±0.15	-40.9±0.1	768.5000	-2.60±0.18	216.8±14.9	731	5	1.78
44.84	46.17±0.26	-8.2±0.1	768.5195	-2.21±0.07	191.7±6.3	729	7	3.02
43.53	44.86±0.05	127.0±0.0	768.6055	-2.27±0.13	201.3±11.4	732	4	1.83
40.77	42.09±0.06	-62.1±0.0	768.4805	-1.99±0.21	185.0±19.9	736	3	0.94
38.93	40.24±0.21	78.5±0.2	768.5469	-1.68±0.04	160.6±3.4	735	9	4.43
25.80	26.86±0.14	129.9±0.1	768.6055	-0.46±0.12	51.3±13.0	737	4	1.83
-24.30	-25.31±0.19	20.0±0.1	768.5117	-0.44±0.05	49.0±5.9	738	6	2.60
-40.72	-42.04±0.23	29.1±0.4	768.5312	-1.41±0.20	131.5±18.5	739	6	2.50

NOTES: Column headings are as defined in Table 3.

image quality, and there are sufficient numbers on different rotations that discrete features do not contribute to the median image.

Tracking the motions of the equatorial features has been very difficult because of their poorly defined boundaries, so that their motions within a single transit cannot be well enough defined to project their positions on a subsequent planet rotation with enough accuracy to convincingly show which feature among several choices is the same one seen on the previous rotation. Fortunately, we found a few cases (as illustrated in Fig. 7) in which neighboring rotations also contain a feature, which resolved the ambiguity. This has also been confirmed by tracking much sharper features in 2003 Keck images of Hammel et al. (2005), which were taken on four successive nights and have relatively high and stable image quality. These two data sets make it quite clear that the equatorial drift rate is relatively small ($\approx 0.5^\circ/\text{h}$ eastward) and has changed little between 2003 and 2011, as illustrated in Fig. 8. Hammel et al. (2005) obtained similar equatorial wind speeds, and pointed out that these

speeds may represent the speed of a wave feature rather than that of the mass motion. The only measurement of the mass flow is the Voyager 2 radio occultation result of Lindal et al. (1987), which is 110 ± 40 m/s eastward ($0.89 \pm 0.32^\circ/\text{h}$). Although this is a rather uncertain value, it does suggest that the equatorial features may be moving slightly westward relative to the zonal mass flow. On earth this phase speed would suggest Rossby waves, but because Uranus is a retrograde rotator, they would move eastward relative to the zonal flow. The more plausible alternative is a Kelvin wave, although it is not clear if the suggested wavenumber and phase speed magnitude are compatible. The magnitude itself is highly uncertain because of the large uncertainty in the radio-derived wind speed.

4.5. Long-lived feature tracking results

A few cloud features on Uranus have extremely long lifetimes, and some have been tracked for years. These include a bright high-altitude cloud feature seen near 30° N (Sromovsky et al. 2007) and the large Berg fea-

TABLE 5
GEMINI-NORTH CORRELATION CLOUD TRACKING RESULTS FROM 23-26 OCTOBER 2011.

PC Lat. (°)	PG Lat. (°)	Longitude (° east)	MJDavg -55000	Drift rate (°/h east)	Zonal wind (m/s west)	ID	<i>N</i>	Δt (h)
63.83	64.87 ± 0.85	284.8 ± 1.1	860.2656	-4.42 ± 0.79	236.9 ± 42.2	222	6	2.02
63.49	64.54 ± 0.71	308.0 ± 1.9	860.2852	-3.74 ± 0.78	202.8 ± 42.6	221	7	3.03
50.00	51.30 ± 0.22	339.9 ± 0.9	860.3242	-3.31 ± 0.35	260.3 ± 27.5	218	9	3.03
49.24	50.55 ± 0.39	244.5 ± 1.2	860.2578	-3.48 ± 0.54	277.9 ± 43.2	219	10	2.27
49.04	50.35 ± 0.40	245.3 ± 1.3	860.2578	-3.31 ± 0.58	265.1 ± 46.9	220	10	2.27
47.56	48.88 ± 0.36	202.9 ± 0.8	859.3359	-2.28 ± 0.41	188.0 ± 33.7	217	5	2.71
44.92	46.25 ± 0.23	206.8 ± 0.8	859.6953	-2.43 ± 0.04	210.9 ± 3.5	216	5	21.30
44.87	46.20 ± 0.30	247.2 ± 0.7	860.2383	-1.38 ± 0.76	119.9 ± 65.7	215	6	1.26
44.06	45.39 ± 0.44	39.9 ± 0.9	860.1875	-2.32 ± 0.04	204.0 ± 3.6	214	7	26.60
43.69	45.02 ± 0.41	39.7 ± 1.0	860.1875	-2.33 ± 0.04	206.1 ± 3.9	213	7	26.60
42.62	43.95 ± 0.25	-24.5 ± 1.0	860.3047	-2.34 ± 0.30	211.5 ± 26.7	212	13	3.03
40.00	41.31 ± 0.35	152.2 ± 0.8	858.6875	-1.70 ± 0.01	159.6 ± 1.1	211	10	50.38
37.05	38.34 ± 0.12	252.8 ± 0.4	860.2695	-0.90 ± 0.14	88.3 ± 14.1	210	12	2.77
34.88	36.14 ± 0.36	-15.9 ± 0.5	860.3477	-0.24 ± 0.68	24.0 ± 68.3	209	5	1.01
30.32	31.49 ± 0.54	52.2 ± 0.7	860.1367	-0.60 ± 0.04	63.3 ± 3.9	208	5	26.60
25.36	26.40 ± 0.17	131.8 ± 0.3	858.9336	-0.44 ± 0.01	48.6 ± 0.7	207	11	50.87
22.45	23.40 ± 0.30	8.3 ± 0.2	860.3320	-0.40 ± 0.18	45.9 ± 20.2	206	8	1.77
21.43	22.35 ± 0.31	7.7 ± 0.2	860.3398	0.08 ± 0.20	-9.5 ± 23.1	205	7	1.51
15.96	16.68 ± 0.33	183.5 ± 0.7	859.6953	0.08 ± 0.04	-9.1 ± 4.2	204	5	21.30
3.65	3.82 ± 0.10	201.4 ± 0.6	859.7773	0.50 ± 0.03	-62.3 ± 4.0	227	4	21.30
3.24	3.39 ± 0.13	331.1 ± 1.9	860.3203	0.32 ± 0.84	-39.4 ± 103.5	226	9	2.52
2.74	2.87 ± 0.22	264.0 ± 0.8	859.3945	0.52 ± 0.01	-64.9 ± 1.2	224	7	72.70
2.27	2.38 ± 0.45	265.0 ± 1.2	860.2422	0.66 ± 0.93	-81.5 ± 114.7	225	6	1.76
2.03	2.13 ± 0.34	242.1 ± 1.5	858.9688	0.52 ± 0.02	-64.1 ± 2.2	223	7	72.95
-30.28	-31.45 ± 0.25	285.4 ± 0.3	860.2852	-0.58 ± 0.08	61.5 ± 8.4	202	13	3.03
-34.60	-35.85 ± 1.40	236.3 ± 0.3	860.0117	-1.55 ± 0.02	156.5 ± 2.5	201	4	20.61

NOTES: Column headings are as defined in Table 3.

ture. The latter feature oscillated between 32° S and 36° S for many years, then began drifting northward in 2005 (Sromovsky and Fry 2005; Sromovsky et al. 2009; de Pater et al. 2011) and dissipated as it approached the equator. Additionally, Sromovsky et al. (2009) were able to track eight features for well over a month (1055-2250 hours) during the intensive equinox observing period. Earlier, Karkoschka (1998) had noted that over the 100 day period covered by his 1997 and 1998 NICMOS observations, all eight of the features he detected were visible whenever they were on the sunlit side of Uranus. Thus we expect at least some of the larger features on Uranus to be trackable over an extended time period.

More recently, another long-lived bright feature near 30° N was tracked from 26 July 2011 until 16 December 2011 (Sromovsky et al. 2012). This is the same feature we identified here with target ID 205 and 206 in the Gemini data set, and manual target ID 14 in the July Keck data set (correlation target 737). When the Keck and Gemini observations are combined together, the time baseline increases enormously and the mean drift rate can be determined with high accuracy. The longitude changed from 128.8°E at JD 55768.7605 to 8.3°E (the 206 value) at 55860.3320, a time difference of 91.5715 days (2197.72 h). In the Keck data set the drift rate is estimated to be $-0.08 \pm 0.03^\circ/\text{h}$, which implies a decrease in east longitude of $176 \pm 66^\circ$ over that time interval. Thus the predicted position in our October Gemini image is at $-47 \pm 66^\circ\text{E}$. The actual position is 8.3°E (mod 360°). Regarding the possibility of 360° multiples being added or subtracted, we find that the only plausible value within the prediction limits is 8.3°E . This implies a drift rate of $(8.3^\circ\text{E} - 128.8^\circ\text{E})/2197.72\text{ h} = -0.0548^\circ/\text{h}$ ($-1.316^\circ/\text{day}$), with an uncertainty of about $0.0007^\circ/\text{h}$

($0.016^\circ/\text{day}$). This highly accurate mean drift rate does not mean that the drift rate did not vary during the time between observations. In fact, Sromovsky et al. (2012) show that the rate did vary after this period.

A second long-lived bright spot was also identified by Sromovsky et al. (2012) at a similar latitude. This feature is present in the July Keck data set, but not seen over a long enough time period to be tracked within that data set. It was tracked in the Gemini data set, and given ID 207, which then was at 26.40°N . Our drift rate of $-0.44 \pm 0.01^\circ/\text{h}$ (or $-10.56 \pm 0.24^\circ/\text{day}$) is somewhat larger than the long term averages of Sromovsky et al. (2012) for this feature, which ranged from -9.125 to $-9.352^\circ/\text{day}$ depending on the period covered. However, it does appear roughly consistent with the average motion of the feature between October and November.

4.6. HST and Gemini observations in 2010

HST observations of Uranus were made in June, July, and August 2010. The June observations provide complete longitude coverage but temporal sampling and the small number of discrete cloud features prevents any wind determination from this data set alone. The July and August observations are part of a SNAP program, and provide neither complete longitude coverage nor suitable temporal sampling for internal wind determinations. We also have November 2010 imaging observations of Uranus from Gemini-North using the NIRI instrument. These also have limited coverage, suffer from poor seeing generally, and don't have adequate temporal sampling for internal wind measurements. However, relying on the long lifetime of most clouds on Uranus, we can combine these data sets to obtain a small number of very precisely determined drift rates. These data sets

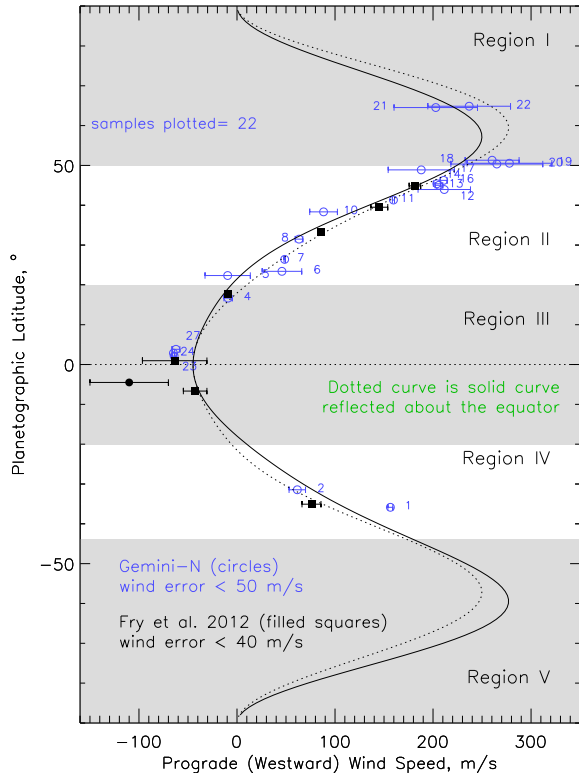


FIG. 6.— Gemini-North wind measurements from October 23-26 2011 (circles) with errors less than 50 m/s, compared to the 10-term Legendre polynomial fit of Sromovsky et al. (2009) (solid curve) and its inverse about the equator (dotted curve). Also plotted are 2009 HST results from Fry et al. (2012) (filled squares) and the Lindal et al. (1987) radio occultation result (filled circle). Numeric labels refer to cloud target IDs given in Table 5.

contain a few cloud features in the northern hemisphere that we attempted to track, even though time gaps were long. However, none of the features could be convincingly demonstrated to have survived over these long intervals and to have had a uniform drift rate. It was always possible to find a drift rate solution when the number of observations was small, but when the number of observations was large, a steady drift solution could not be found.

5. LEGENDRE POLYNOMIAL FITS AND SYMMETRY PROPERTIES

5.1. Fitting methodology

To provide a smooth profile for use by atmospheric modelers and other researchers, we carried out Legendre polynomial fits to combinations of observations from 2009 and 2011, which includes 30 points, and to a more extensive set of observations that also included the highest accuracy observations from 2007, which contains an additional 28 points. We fit the angular (longitudinal) drift rates, rather than wind speeds because the observations are most consistent with a constant angular drift rate at high latitudes. The longitudinal drift rate does not change as dramatically at high latitudes as does the wind speed, and thus is much easier to fit without generating violent deviations at other latitudes where data are more sparse. To limit large deviations in the sparsely sampled regions, we also limited the order of the poly-

nomials to 11th order (12 terms) for the 2009-2011 data set, and to 13th order (14 terms) for the 2007-2011 data set. We also added the 1986 Voyager measurement at 71° S (Smith et al. 1986) and artificial measurements of $4.3^\circ/\text{h}$ westward at both poles to better constrain high latitudes. The angular rate $4.3^\circ/\text{h}$ was chosen to be consistent with the nearest observed values shown in Fig. 9A. The Voyager point was not needed for fits that were constrained to be symmetric. Because both of these fits are more symmetric than the fit we obtained to the 2007 data alone, we also considered it possible that the circulation of Uranus is actually close to symmetric, and carried out fits in which only the even Legendre polynomials were used, insuring fits that were symmetric about the equator.

We modeled longitudinal drift rates and wind speeds using the following Legendre expansion and conversion equations:

$$d\phi/dt = \sum_{i=0}^n C_i \times P_i(\sin(\theta)) \quad (3)$$

$$U = 4.8481 \times 10^{-3} R(\theta) \times d\phi/dt \quad (4)$$

$$R(\theta) = R_E / \sqrt{1 + (R_P/R_E)^2 \tan^2(\theta)^2} \quad (5)$$

where C_i are the coefficients given in Table 6, $P_i(\sin(\theta))$ is the i th Legendre polynomial evaluated at the sine of planetographic latitude θ , $d\phi/dt$ is the westward longitudinal drift rate in $^\circ/\text{h}$, U is the wind speed in m/s, R is the radius of rotation in km at latitude θ , which is the distance from a point on the 1-bar surface to the planet's rotational axis, R_E and R_P are the equatorial and polar radii of Uranus. For the symmetric fits, the summation over i is only over the even polynomials. The model coefficients are found by minimizing χ^2 , but with error estimates for the observations modified as described in the following paragraph.

Because very accurate measurements of drift rates at nearly the same latitude often did not agree within their uncertainties, and often differed by many times the value expected from those uncertainties, it is clear that one of the following possibilities must be considered: (1) the circulation is not entirely steady, or (2) that the features that we measure do not all represent the same atmospheric level, or (3) the cloud features we track are not always at the same latitude as the circulation feature that is moving with the zonal flow. Examples of the latter possibility are the companion clouds to Neptune's Great Dark Spot, which traveled with the spot even though separated by nearly 10° in latitude (Sromovsky et al. 1993). Less extreme examples have also been seen on Uranus (Hammel et al. 2009; de Pater et al. 2011). If we include highly accurate measurements, and weight them by their estimated accuracy, they can dominate the fit, leading to unreasonable variations in regions where there are less accurate measurements. Since these high accuracy measurements clearly do not all follow the mean flow, we must add an additional uncertainty to characterize their deviations from the mean flow. We do this by root sum squaring the estimated error of measurement with an additional error of representation. We adjust the size of this error until the χ^2 value of the complete asymmetric fit is approximately equal to the number of degrees of freedom (number of measurements minus the number of

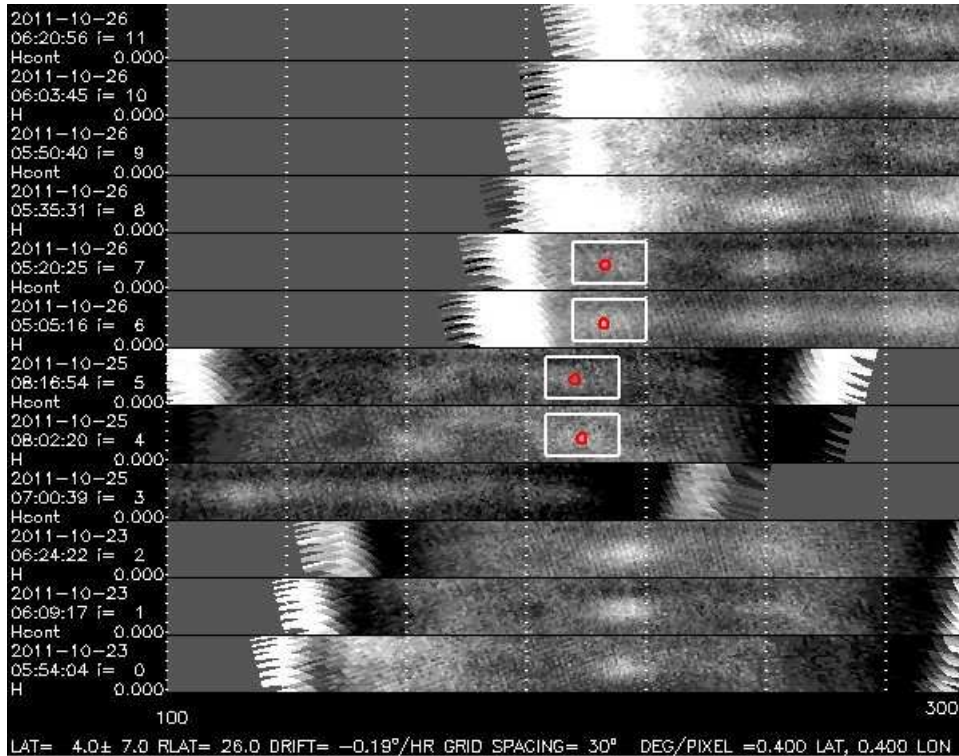


FIG. 7.— Diffuse equatorial features illustrated in this stack of rectilinear projections of median subtracted 2011 Gemini NIRI images from 23 October (bottom three strips), 25 October (next three strips), and 26 October (top six strips). The boxes outline the same feature that appeared on successive rotations. Also note the pattern of roughly 40° separation between equatorial features.

fitted parameters). This representative error (referred to as *reper* in the figure legends) turns out to be approximately $0.1^\circ/\text{h}$ for both the 2009-2011 and 2007-2011 data sets.

5.2. Fit results

With the constraints described above, we obtained the fits given in Fig. 9 for the 2009 and 2011 data sets combined and in Fig. 10 for the 2007, 2009, and 2011 data sets combined, with fit coefficients, *reper*, and χ^2 values listed in Table 6. The χ^2 uncertainties for both of these fits are larger than the difference in their χ^2 values, confirming that these data sets cannot distinguish between symmetric and asymmetric models. We also combined the data from 1997 through 2005 (see Sromovsky et al. (2009) and references therein), selecting only those with wind errors < 10 m/s and latitude errors $\leq 0.5^\circ$, and then combined these with the high-accuracy winds from 2007-2011, which yielded a total of 125 observations (127, including synthetic polar points). Fits to this combination are shown in Fig. 11, with coefficients provided in the last two columns of Table 6. In this case the asymmetric fit is far superior to the symmetric fit, with χ^2 being smaller by 77, which is 3.4 times the expected uncertainty of $\sqrt{2} \times 16$ in the χ^2 difference.

5.3. Symmetry properties

A comparison of the asymmetry properties of the 2007-2011 observations and those of the earlier observations is provided in Fig. 12. The new fits are more symmetric than prior fits, and the fit that is constrained to be symmetric is very close to the northern hemisphere fit of the complete fit because there are more points in the northern hemisphere. However, though the addition of new

observations makes the entire data set somewhat more symmetric, the remaining asymmetry is better defined. It is not clear whether the true asymmetry of the zonal winds has changed slightly or whether the new observations are just sampling a different statistical variation in target motions. The better definition of asymmetry obtained from the larger combined data set depends on the earlier observations, which are better distributed in latitude and contribute more measurements in the southern hemisphere. The large berg feature is responsible for many of those observations; as it traveled from $33\text{-}34^\circ\text{S}$ to 8°S (Sromovsky et al. 2009; de Pater et al. 2011), it provided samples of drift rates within that range, though unfortunately sampled too sparsely to provide a detailed profile.

It is clear that because high-accuracy winds do not always represent the mean zonal flow with similar accuracy, the asymmetry information in a sparsely sampled data set can easily be misleading. With large numbers of samples, which we obtained by combining all observations from 1997 onward, this is less of a concern. By combining observations between 1997 and 2005 with those up to 2011, we are not too far from representing the circulation pattern near the 2007 equinox (the mean year of these observations is ≈ 2006). If the asymmetry is actually a long-delayed seasonal effect (with a phase shift near 90°), then it should be reflected about the equator at the prior equinox, and near the midpoint of the transition in the 1986, when Voyager observations were made. However, as shown by the Voyager results plotted in Fig. 12B (open circles) it does not appear that the 1986 Voyager measurements are measurably different from our grand average profile, nor from the 2007

TABLE 6
 LEGENDRE POLYNOMIAL FITS TO COMBINED HIGH-ACCURACY DRIFT RATES FROM 1997-2011 OBSERVATIONS.

Order	Coefficients (2009-2011)		Coefficients (2007-2011)		Coefficients (1997-2011)	
	Even+Odd	Even only	Even+odd	Even only	Even+odd	Even only
0	1.21686239	1.21686239	1.25118116	1.25328423	1.24197012	1.25037831
1	0.12285565		-0.02175064		-0.02848715	
2	3.59459637	0.12285565	3.69171880	3.71892507	3.69457598	3.72050211
3	0.07697320		0.07015199		0.08752786	
4	0.30820520	3.59459637	0.13362164	0.11135703	0.15287708	0.12041514
5	-0.42303760		-0.13169439		-0.13202142	
6	-0.49582428	0.07697320	-0.62305001	-0.68903134	-0.65646542	-0.73555624
7	0.03484260		-0.05877913		-0.08292523	
8	-0.54870970	0.30820520	-0.39623823	-0.42572871	-0.31793598	-0.34206461
9	0.10603441		0.01148944		0.09172810	
10	0.21759050	-0.42303760	0.30751536	0.28876768	0.15934681	0.20553095
11	0.07569097		0.01664328		0.06504432	
12			-0.05641039	0.04557578	0.02752308	0.08364616
13			0.12180474			
NF:	27	33	53	60	121	127
reperr	0.109°/h	0.109°/h	0.105°/h	0.105°/h	0.090°/h	0.088°/h
χ^2	27.16	33.90	53.15	62.92	121.34	198.065
χ^2/NF	1.006	1.027	1.003	1.049	1.003	1.560
$\sigma_{\chi^2/NF}$	0.27	0.25	0.19	0.18	0.13	0.13

Note: To limit oscillations in poorly sampled regions, all fits make use of a 71°S observation by Voyager 2 and fix the drift rate at both poles to be 4.3°/h westward. NF (number of degrees of freedom) is the number of measurements minus the number of fitted parameters. The representativeness error (reperr) is discussed in the text.

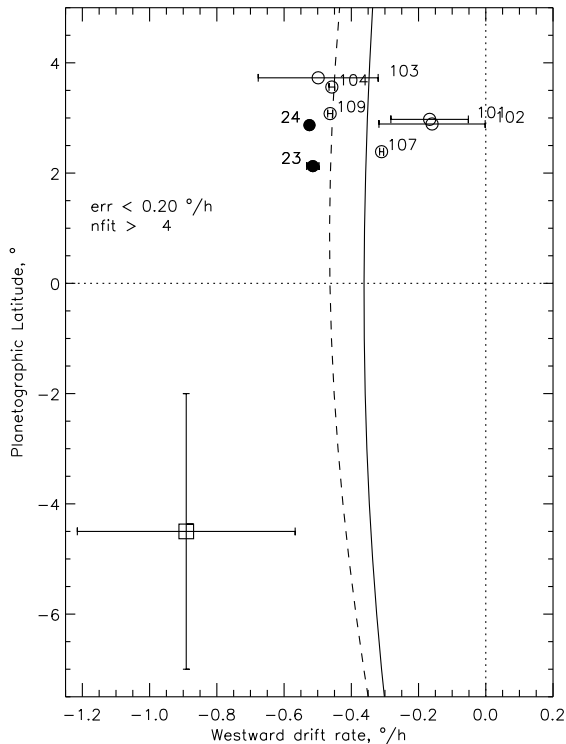


FIG. 8.— Comparison of low-latitude wind measurements in 2011 Gemini images (filled circles) with measurements in 2003 Keck images (open circles) and the Lindal et al. (1987) radio occultation measurement (square), for which the vertical error bar here represents the range of latitudes sampled by ingress and egress measurements on which the wind determination is based. The solid curve indicates the 10-term Legendre polynomial fit of Sromovsky et al. (2009), while the dashed curve is our 13-term fit described in Section 5.2.

equinox results alone (Sromovsky et al. 2009). This further enhances the probability that the asymmetry may be a relatively stable feature over a long period, perhaps more than a uranian year. While this seems to violate our expectations of symmetry in the annual average (over the uranian year), there are other examples of persistent asymmetry in zonal circulation profiles, namely those of Jupiter and Saturn.

There are alternative interpretations, however, for the lack of change in asymmetry of the wind profile. For example, if the phase shift is closer to 45° and had a sinusoidal variation, then the asymmetry be be the same at both equinox and solstice, with maxima in between. Another possibility is that the symmetry variation does not proceed in a uniform or sinusoidal fashion, but achieves most of the change by the solstice, and changes little between solstice and the next equinox. Further observations over many years will be required to distinguish these possibilities.

6. POLAR CLOUD FEATURES

6.1. North polar projections

The 2011 Keck observations provided the best views to date of the north polar region of Uranus. This is best illustrated by polar stereographic projections of the northern hemisphere that we assembled from 85 images taken on 26 July 2011 and 4 images from 27 July 2011. To combine together images taken at different times during the rotation of the planet we had to account for the advection of features by the zonal wind over the time interval between images. This is a significant effect within the north polar jet, where wind speeds exceed 250 m/s and longitudinal drift rates exceed 5°/hour. In Fig. 13 we display two polar stereographic projections, one with the image brightness proportional to I/F (left) and the same image with a 25-pixel box car smoothed image subtracted

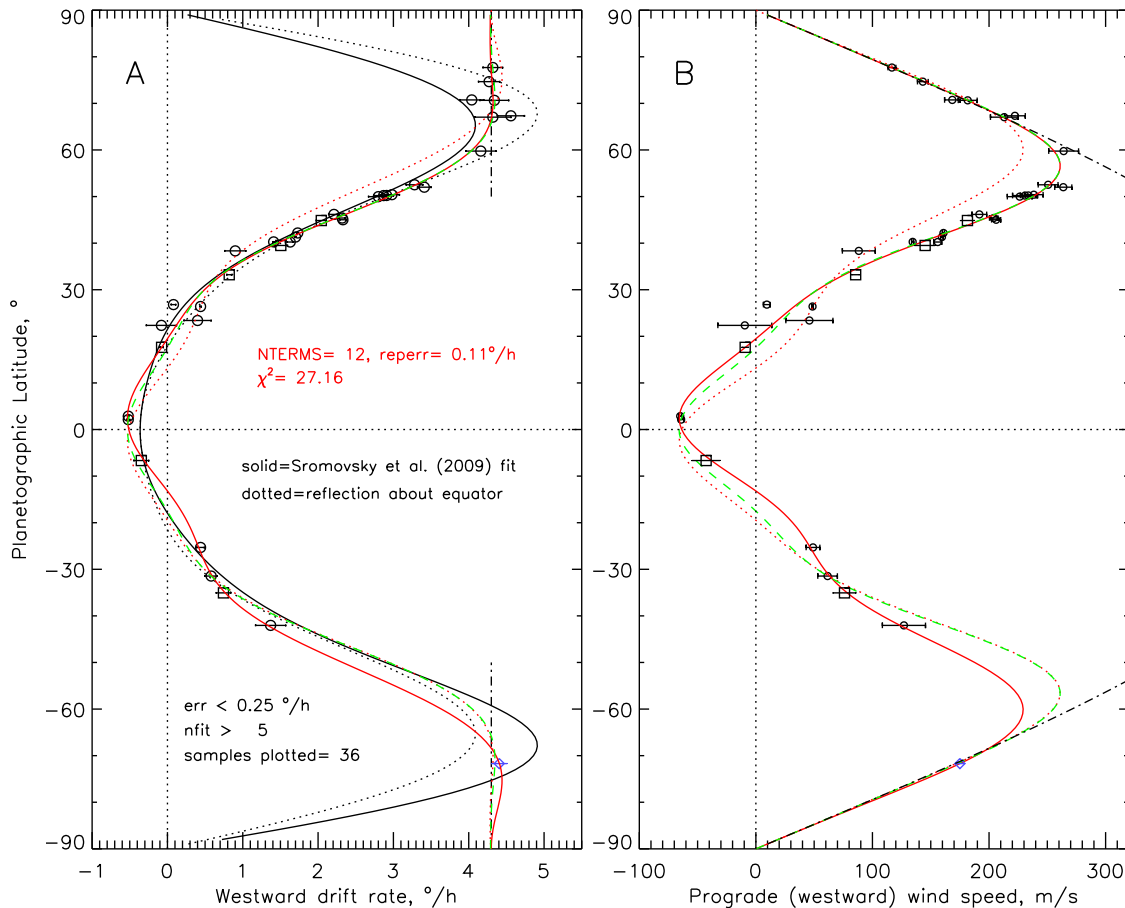


FIG. 9.— A: Combined 2009 HST observations and 2011 Keck and Gemini observations of longitudinal drift rates, filtered as indicated in the legend, compared to the Sromovsky et al. (2009) fit to 2007 observations (black solid and dotted curves for fit and inverted fit respectively), and to a 12-term Legendre polynomial fit to the 2009-2011 observations (red solid and dotted curves for fit and inverted fit respectively) and to an even order (6-term) symmetric fit (dashed green curve). The dot-dash lines indicate solid body rotation rates of $4.3^\circ/\text{h}$ westward relative to the longitude system. The χ^2 value is for the asymmetric 12-term fit. See Table 6 for additional statistical information, which shows that the symmetric and asymmetric fits are equally good for this case. B: Corresponding observations and fits converted to zonal wind units.

(right). In the left hand image latitudinal variations in brightness are much larger than variations due to local cloud features, while in the high-pass filtered version, the local cloud features are revealed in striking detail. The stretch used in the filtered image is just -20 to 40 DN, while in the unfiltered image it is 2000-5000 DN, a factor of 50:1. Thus the small cloud features visible in the filtered image produce brightness variations that are only a few percent as large as the latitudinal variations.

The distribution of the small bright features is relatively uniform over the upper left quadrant of the polar mosaic. The decline in numbers of bright features in the other quadrants may simply be a result of fewer images contributing there. These are also regions where the shape of discrete features becomes more distorted by shear in the wind profile. The real features don't get sheared, but the zonal wind shift application causes an artificial distortion that will reduce contrast. The importance of shifting image pixels to account for the zonal wind profile is illustrated in Fig. 14, where the left mosaic was assembled with no wind shift, while the right was assembled with the nominal wind shift (the 13-term fit in Table 6 for the 1997-2011 observations).

Polar projections of Gemini-North images are dis-

played in Fig. 15, which shows a 33-image average for the H filter and a 64-image combination for the Hcont filter on 26 October 2011. Both filters show the same discrete feature structure in the polar regions, but not as fine a detail as displayed by the Keck polar composite. Thus, each feature in the Gemini composite is likely a blurred mix of several features of somewhat smaller scale. Both filters display the same pattern of features, proving that they are not due to random noise fluctuations. Applying the same technique to Gemini NIRI images obtained on 25 October revealed no discrete polar features. Although we had only 19 H images and 18 Hcont images to combine for that day, the lack of features is more likely due to the lower seeing quality. On 25 October, the natural seeing (given by the header keyword AOSEEING) was generally in the 0.5-1 arcsecond range, while on 26 October, the seeing was much more stable and for almost every image was below 0.4 arcseconds. Although the 26 July 2011 Keck seeing was worse, generally in the 0.6-1.2 arcsecond range (at $0.5 \mu\text{m}$), the ability of the Keck AO system to use the planet as a wavefront reference (VMAG=5.5) instead of a satellite (VMAG=13.7-14.2) allowed it to produce more detailed images than was possible with the Gemini AO system

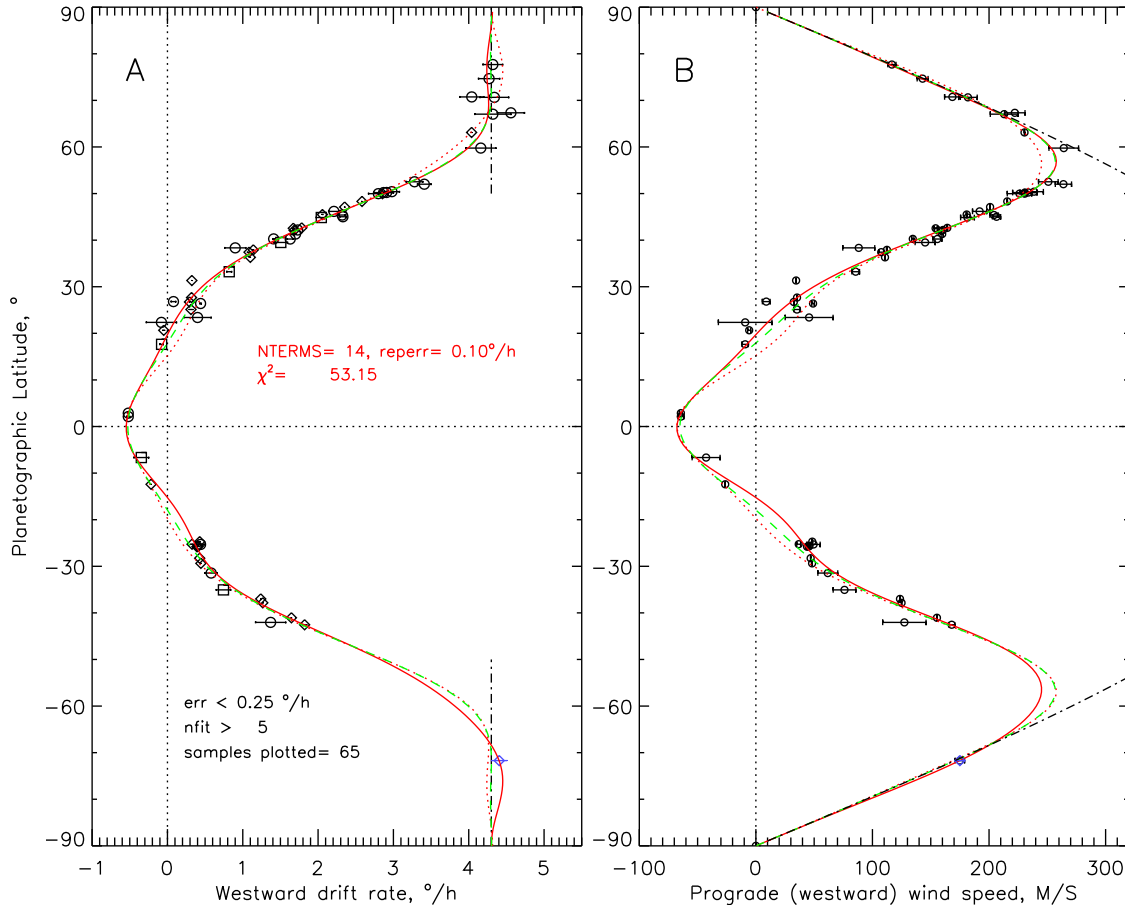


FIG. 10.— As in Fig. 9 except that we here combined 2009 HST observations and 2007-2011 Keck and Gemini observations and carried out a 14-term Legendre polynomial fit to the 2007-2011 observations. Here we omitted the Sromovsky et al. (2009) fit for clarity. Again, the symmetric and asymmetric fits are of indistinguishable quality.

under superb natural seeing conditions. Another virtue of the Keck AO system is that AO correction deteriorates with angular distance from the wavefront reference to the target (de Pater et al. 2004), which is generally larger for a satellite than for the planet itself.

6.2. Styles of northern cloud features

While the polar projection image is dominated by zonal bands and zonally streaked features south of about 60°N , at higher latitudes the dominant feature style is small bright spots and a smaller number of small dark spots. This morphology is similar to what is seen at high polar latitudes on Saturn (West et al. 2009), where such features were likened to terrestrial cumulus convective clouds. A Cassini image of Saturn’s north polar region, shown in Fig. 16, bears a striking resemblance to the north polar region of Uranus, as shown in Fig. 14. On Saturn, both polar regions can display these features at the same time, even when the two polar regions are in opposite seasons. In January 2009, which was close enough to Saturn’s August 2009 equinox that both polar regions were partially illuminated, Cassini took images (PIA10583 and PIA10585) revealing small scattered bright spots in both the spring-time (north) polar region and in the fall (south) polar region. Uranus’ polar regions, on the other hand, are very asymmetric, as will be shown in the next section.

While the uranian features bear a superficial resem-

blance to fair weather cumulus cloud fields on earth, the scale is much larger. The spacing between the Uranus polar features is typically $5\text{--}10^\circ$ in longitude and $3\text{--}5^\circ$ in latitude. The typical size of the cloud elements is 1° in latitude and 3° in longitude. The latitudinal extent of the features corresponds to a physical distance of ~ 450 km. The saturnian features are typically somewhat smaller (~ 200 km). The optical depth of uranian bright cloud features is not well known, and how much less optical depth is present in the dark regions is completely unknown. The fact that none of these features is visible in K' images, means that they are deeper than the methane condensation level near 1.2 bars, which is confirmed in a later section by comparison of H and Hcont images. The few bright polar features we could analyze do not appear to be optically thick, making it less likely that they are deep convective features. On the other hand, it is possible that our images have not resolved these features, which would reduce their apparent I/F values and their apparent optical depths. The saturnian features appear very opaque in $5\text{-}\mu\text{m}$ images, implying that they are optically thick.

6.3. Comparison of north and south polar regions

Although post-Voyager imaging has failed to reveal any discrete clouds in the south polar region of Uranus, there remained a small possibility that subtle features were present but not seen because of insufficient S/N.

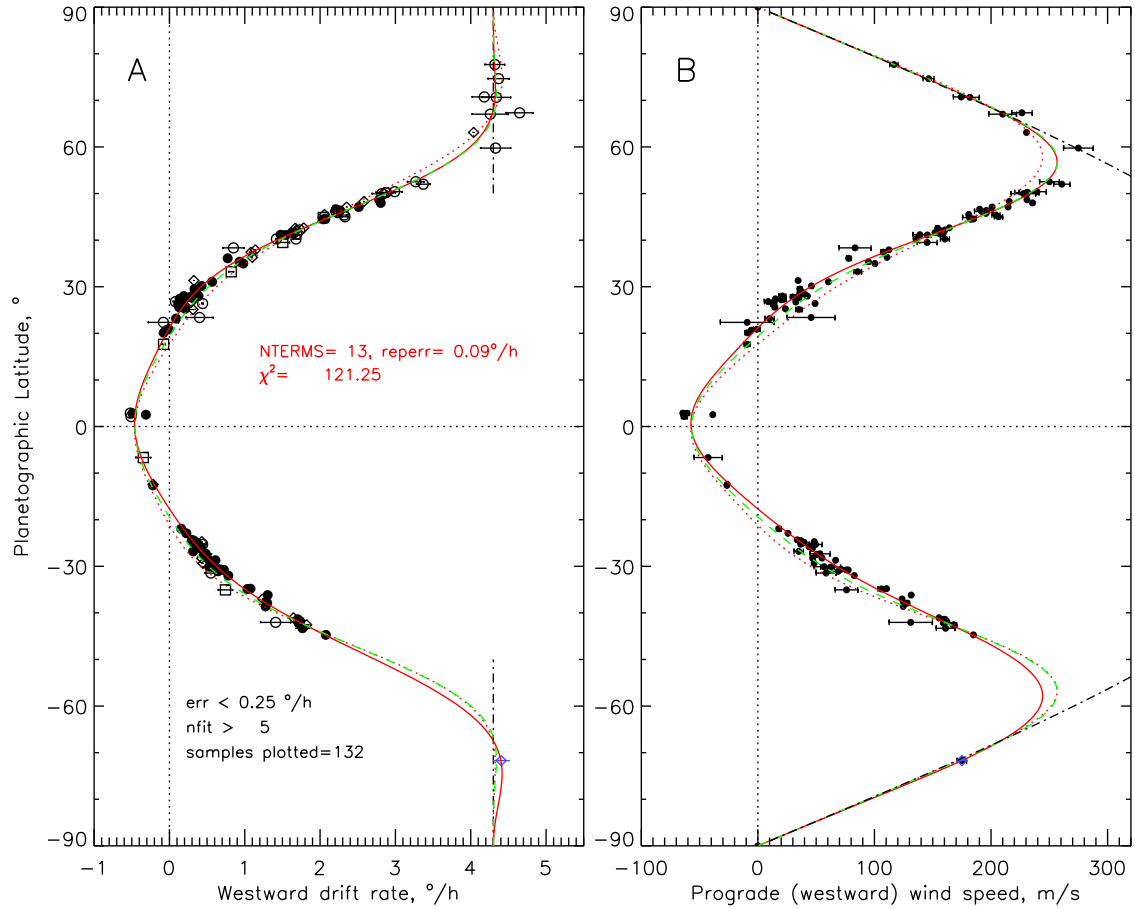


FIG. 11.— As in Fig. 10 except that we here combined 1997-2005 HST and Keck observations with 2009 HST observations and 2007-2011 Keck and Gemini observations and carried out a 13-term Legendre polynomial fit. For this data set, Table 6 shows that the asymmetric fit is significantly better than the symmetric fit.

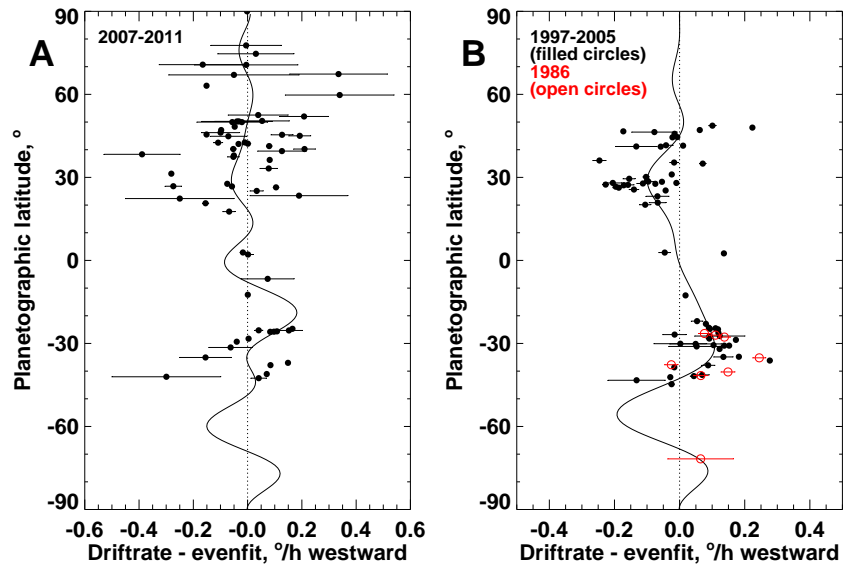


FIG. 12.— A: Using the symmetric fit of the 2007-2011 observations as a reference and subtracting it from everything plotted, the non-symmetric fit to those observations appears as the solid curve and the individual observations from that data set as filled circles. B: As in A except that the filled circles are from the 1997-2005 data set, open circles are 1986 Voyager results Smith et al. (1986), and the asymmetric fit is to the largest (1997-2011) data set.

To address that issue we gathered high quality images from 2003, and formed a south polar mosaic using the

same wind shift approach used for the north polar mosaic. While we didn't have as many images to work with,

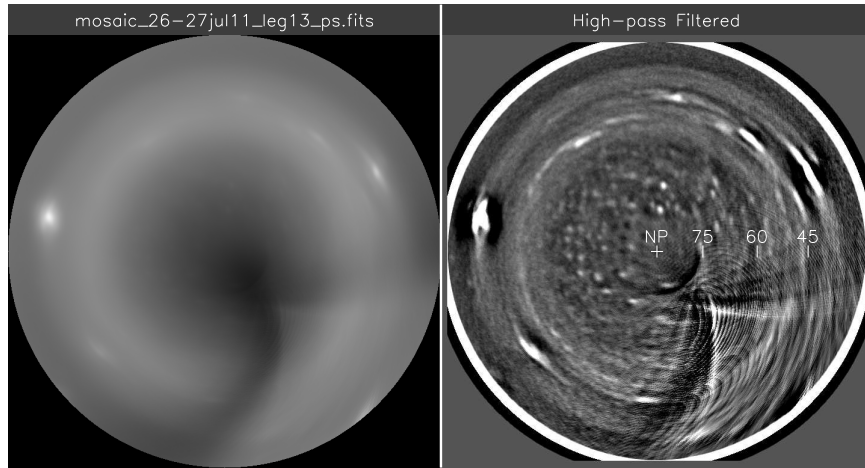


FIG. 13.— Left: polar projection of Keck NIRC2 H-band images of Uranus, blended together by shifting longitudes in proportional to the 13-term Legendre fit. Right: a high-pass filtered version of the left image obtained by subtracting a 25-pixel boxcar smoothed version from the original image. The displayed brightness range for the filtered image is 50 times smaller than for the unfiltered image. Both cover the range from 30°N to 90°N .

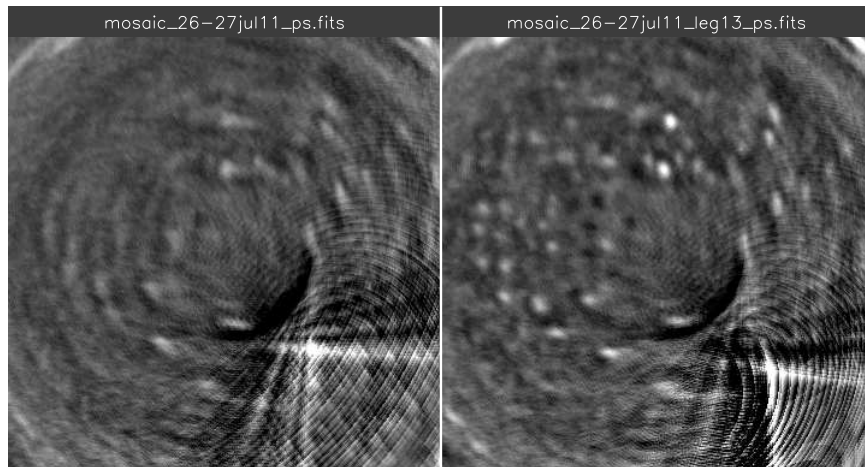


FIG. 14.— Left: Blowup of a polar projection mosaic of Keck NIRC2 H-band images of Uranus, blended together assuming zero wind speed and high-pass filtered with a 25×25 pixel boxcar. Right: X2 blowup of the same polar projection mosaic obtained by shifting longitudes in proportion to the individual displacements predicted from the 13-term Legendre fit.

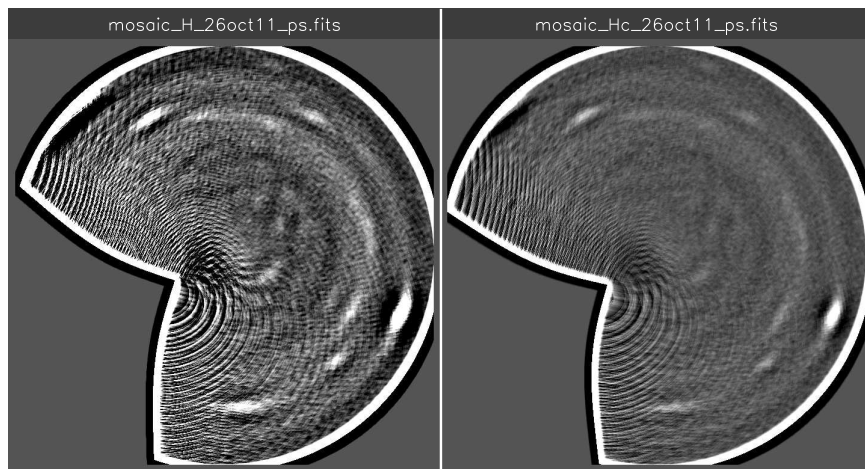


FIG. 15.— Left: Gemini-North H filter polar stereographic projection from 30°N to 90°N mosaic average of 33 images. Right: as at left, except for use of 64 Hcont images. Both are shown with high-pass filtering obtained by subtracting a $25\text{-pixel} \times 25\text{-pixel}$ boxcar smoothed version from each. Each image is $720\text{ pixels} \times 720\text{ pixels}$.

the quality of individual images was generally higher because the AO system was better adjusted and the seeing

may have been better. The result for mosaicking the three H images from 4 October is shown in Fig. 17. In



FIG. 16.— Cassini ISS WA image of Saturn’s north polar region on 2 January 2009, when it resembled the North polar region of Uranus. This image was taken through a clear filter at a distance of 895 000 km to Saturn’s center and at a phase angle of 59° . The size of a single pixel is about 100 km. Grid spacing is 10° in latitude and 30° in longitude. The image is spatially filtered to enhance small scale contrast using an unsharp mask in which the raw image is high-pass filtered with a box-car smoothing over 13 pixels, then 5 times that filtered image is added back to the original image. The large donut feature is at 68°N , where 1° of longitude is 325 km and 1° of latitude is about 950 km. The most numerous small features are only about 200 km in diameter.

the overlap region where all three images contribute to reduce noise levels (roughly a 100° region centered at 7 o’clock), there is no indication of any discrete cloud feature standing above the noise level. This should be compared to the north polar mosaic displayed in Fig. 13. There is certainly no feature in the south polar region with the contrast found in the north polar region in 2011. Instead, the south polar region seems devoid of discrete cloud features, but has (or at least had in 2003) a banded structure that is currently not seen in the north polar region. A south polar mosaic created without accounting for zonal wind shift produced an image that is virtually identical to the one produced with the wind shift. Neither showed any small discrete features. Even better views of the south polar region, provided by HST images from 1994–2000 Rages et al. (2004), also failed to reveal any discrete polar cloud features.

Although the observed polar asymmetry on Uranus might be unrelated to seasonal forcing, as perhaps is the case for the wind asymmetry, a seasonal cause for the polar asymmetry is certainly the most plausible. If it is a seasonal effect, then a few years after the next equinox, when the south polar region will again come into view, we would expect it to look like the north polar region looks now, and just before that equinox we would expect the north polar region to be devoid of discrete cloud features. As we continue to observe the north polar region for the next four decades, at some point the convective activity should stop, and a polar cloud cap should form (Hammel and Lockwood 2007). Exactly when these transitions will take place and what detailed mechanisms are involved in this expected response to seasonal forcing remain to be determined.

The dramatically different appearance of the two polar regions of Uranus is a possible indication of different stability structures of the atmospheres. Karkoschka and Tomasko (2009) reported reduced methane mixing ratio at high southern latitudes, based

on 2002 STIS spectra. This finding was confirmed by Sromovsky et al. (2011), who also found the depletion to be relatively shallow (only down to a few bars). These results suggested a meridional flow of gas from low latitudes upward through the methane condensation level, where condensation reduces the methane mixing ratio, transport of that depleted gas to high latitudes, and then descent of the depleted gas, which reduces the average methane mixing ratio to the observed levels. Such a circulation would tend to suppress convection in the region of down-welling gas, which is consistent with the absence of any discrete convective features in the south polar region in 2003. Although this is suggestive, the real reason for lack of convection in the south might be due to increased thermal stability produced by some other mechanism that alters the thermal structure in this region, which itself might have a seasonal origin. It is worth noting that there are occasions when convective storms can occur in regions of general downwelling. On Jupiter, for example, thunderstorms occur primarily in belts (Showman and de Pater 2005).

The meridional flow suggested above for the upper troposphere, is opposite to the direction of heat transport required to reduce the temperature difference between equator and pole. According to Friedson and Ingersoll (1987), the average annual solar energy absorbed by the poles exceeds that absorbed at the equator, and radiative convective models suggest that the poles should be ~ 6 K warmer than the equator, which significantly exceeds the 2.5 K obtained with meridional transports included. If northern poleward meridional transport of methane is occurring in the upper troposphere and southward transport is occurring somewhat deeper, that suggests that most of the heat transport is occurring in the return flow. But deeper still, another poleward transport is suggested by microwave observations down to the 50-bar level (Hofstadter et al. 2004), where microwave absorbing gases (NH_3 and H_2S) seem to be symmetrically

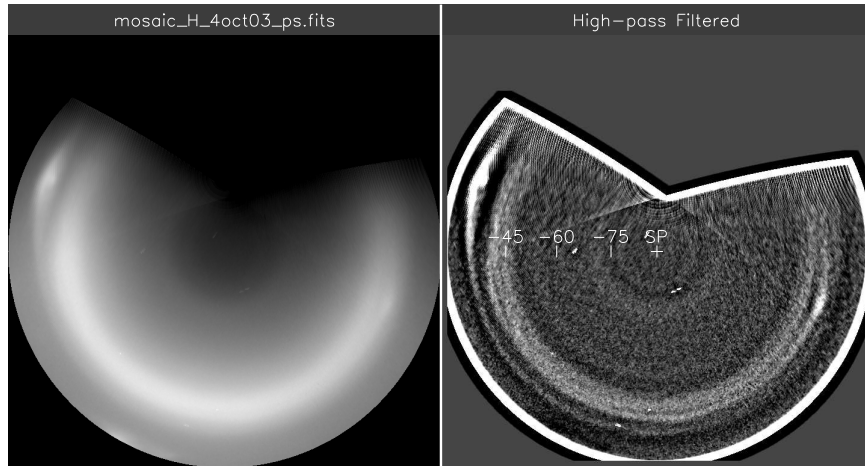


FIG. 17.— Left: South polar projection of Keck NIRC2 H-band images of Uranus obtained on 4 October 2003, blended together by shifting longitudes in proportional to the 10-term Legendre fit wind profile of Sromovsky et al. (2009). Right: a high-pass filtered version of the left image obtained by subtracting a 25-pixel boxcar smoothed version from the original image, which is 720 pixels on a side. The displayed brightness range for the filtered image is 30 times smaller than for the unfiltered image. Both cover the range from 30°S to 90°S.

depleted in both polar regions.

7. VERTICAL STRUCTURE

7.1. *The spatial modulation method*

An estimate of the pressure levels of many of the discrete cloud features can be made using the ratio of spatial modulations in H and Hcont filters, as employed in the simplest form by de Pater et al. (2011) and in a somewhat more exact form by Sromovsky et al. (2012). These two filters not only have different penetration depth profiles (Fig. 1) over a useful pressure range, but they also have sufficiently similar effective wavelengths that we can ignore wavelength dependent differences in seeing or effective spatial resolution, which can distort the observed modulation ratios and the inferred cloud pressures. The similarity in spatial resolution is only valid if the seeing is stable over the time span covered by the H and Hcont images.

Fig. 1 displays the I/F obtained when a unit-albedo surface is placed at different depths within a model aerosol-free Uranus atmosphere. For a given filter, the apparent (externally viewed) I/F of a unit albedo surface at pressure P approaches its asymptotic value as P becomes arbitrarily large (which yields the same I/F as for a clear atmosphere) at a rate that depends on the degree of absorption within the filter band. The I/F difference from the asymptotic value indicates how sensitive the filter is to spatial modulations in cloud reflectivity or amount as a function of where they occur in pressure. In the simplest case of a small isolated cloud feature, the modulation can be thought of as simply the difference between the peak I/F of a cloud feature and the I/F of its surroundings. The useful pressure range for H and Hcont is between 300 mb and 4-5 bars, between which the I/F differences in H decline more rapidly with pressure than the I/F differences in Hcont. The ratio of H modulations to Hcont modulation thus provides a measure of the pressure location of the modulations.

In applying the spatial modulation technique to our observations, we followed Sromovsky et al. (2012) in calculating model ratios for middle latitudes for an array of cloud pressures and view angles including the effects of the main cloud layer between 1.2 and 2 bars

(Sromovsky et al. 2011). The discrete cloud is treated as a physically thin perturbation inserted into the background structure. Both the background and discrete perturbations are modeled as conservative Mie particle layers of $0.8 \mu\text{m}$ in radius with a refractive index of 1.3. An effective pressure for the discrete cloud can be inferred from the ratio of spatial modulations in I/F (see Fig. 15 of Sromovsky et al. 2012). From the peak-to-peak amplitude in modulations we can infer the change in optical depth required. If the cloud feature is not spatially resolved, the inferred optical depth maximum will be less than the true optical depth.

7.2. *Cloud structure results*

A sample application of the modulation ratio technique to target 3 in Table 7 is provided in Figs. 18 and 19. A target box size is selected and positioned in the Hcont image (shown twice in Fig. 18, once without and once with high-pass filtering). The corresponding target box in the H image is shifted slightly as needed to maximize correlation between Hcont and H variations. This shift is usually no more than a fraction of a degree of longitude and less than a few tenths of a degree latitude. Once the correlation is maximized, we fit a straight line to the H vs Hcont I/F variations within the target box to determine the slope (see Fig. 19) at the view angles of the observations. We then use a spline interpolation of the model slope vs. pressure and view angles to infer a pressure from the observed slope. From the pressure we interpolate the models of I/F vs optical depth to infer the optical depth change that would yield the observed variation of I/F at the observed view angles. For target 3 in Fig. 18 the effective pressure is 1.17 ± 0.02 bars (formal error), and the optical depth variation is 0.15, with negligible formal uncertainty. Note that I/F gradients defined by the boundary of the target box are subtracted from the gradients within the box to keep background variations from affecting local changes.

The inferred pressure of modulation is affected by the relative calibration error between the H and Hcont images. Our analysis measures the central disk value of each image and then converts the image to I/F units by a scale factor that produces a central disk I/F equal

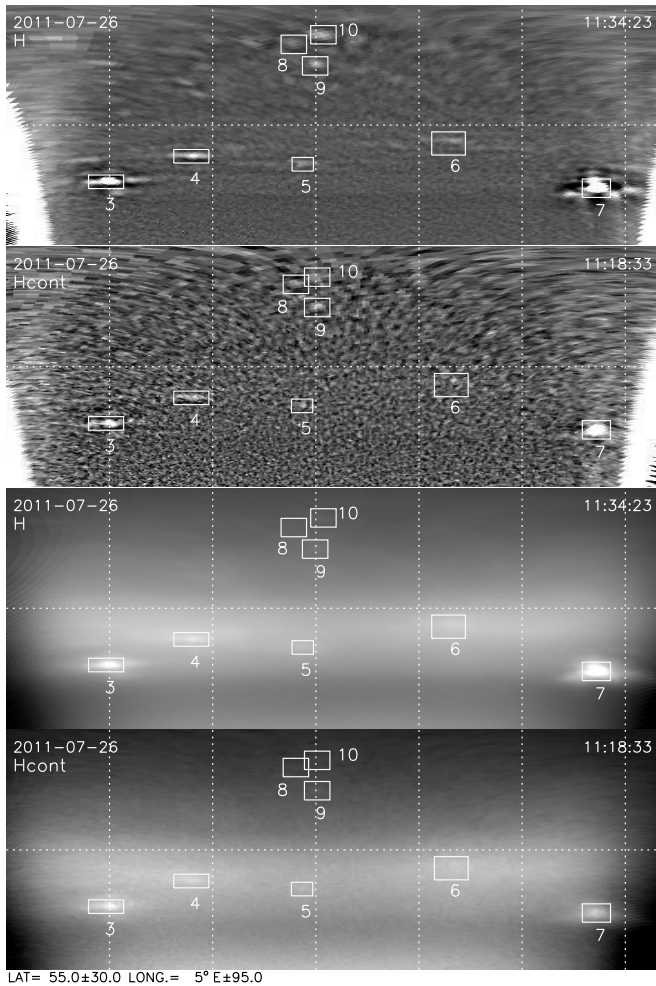


FIG. 18.— Rectilinear projection of NIRC2 NA images of northern cloud features on 26 July 2011, covering longitudes from -90°E to 100°E and latitudes from 25°N to 85°N , with labeled outlines indicating target boxes for analyzing spatial modulations. ID numbers refer to rows in Table 7. The top two images are high-pass filtered versions of the bottom images, which display local discrete cloud variations more clearly. Note that the S/N ratio of the Hcont image limits the number of high latitude features for which a pressure estimate can be obtained.

to previously determined I/F values. New central disc measurements using preliminary calibrations of 2011 Gemini-North images, indicate significant changes from those of Sromovsky and Fry (2007). The new values are 0.86×10^{-2} (H) and 2.9×10^{-2} (Hcont) with relative errors of 5% and 10% respectively. The effect of a 10% increase in the ratio of H to Hcont on derived pressures in a typical example is to decrease P by about 100 mb and to increase the derived optical depth by 30%. Thus the formal uncertainties given in Table 7 are generally less significant than the uncertainties associated with relative calibrations, which add about 0.1 bars to the pressure uncertainty and 30% to the optical depth uncertainty. There are also bias errors associated with unresolved cloud features, for which apparent optical depths will be lower than actual values.

The results in Table 7 are also plotted in Fig. 20, where we see that most clouds reside deeper than the 1.2-bar methane condensation level, including the broad equatorial features and all the compact polar cloud features for which we could estimate the pressure. Bright spots

TABLE 7
SUMMARY OF DISCRETE CLOUD PARAMETERS FOR 26 JULY 2011 (1-12) AND 26 OCTOBER 2011 (A-F).

PID	TID	PCLat	PGLat	Elon	P, bars	Optical depth
1		3.80	3.98	-6.2	$1.64^{+0.16}_{-0.13}$	0.101 ± 0.01
2		3.00	3.14	39.0	$1.97^{+0.31}_{-0.23}$	0.116 ± 0.04
3	21	40.8	42.12	-61.0	$1.12^{+0.02}_{-0.02}$	0.145 ± 0.001
4	20	47.2	48.52	-36.2	$1.24^{+0.09}_{-0.06}$	0.076 ± 0.002
5	5	45.2	46.53	-4.0	$1.75^{+1.2}_{-0.4}$	0.058 ± 0.4
6	18	50.4	51.70	39.4	$1.38^{+0.22}_{-0.14}$	0.066 ± 0.01
7	13	39.2	40.51	81.6	$0.88^{+0.02}_{-0.02}$	0.156 ± 0.001
8		75.6	76.23	-5.8	$3.66^{+6.3}_{-1.4}$	1.000 ± 0.05
9		69.8	70.65	0.4	$1.77^{+0.95}_{-0.36}$	0.054 ± 0.2
10		77.4	77.95	0.4	$1.49^{+0.80}_{-0.22}$	0.033 ± 0.04
11		77.2	77.76	0.0	$1.51^{+0.60}_{-0.20}$	0.035 ± 0.025
12		69.8	70.65	0.2	$1.86^{+1.2}_{-0.4}$	0.060 ± 0.2
A		45.6	46.93	227.8	$1.61^{+0.38}_{-0.21}$	0.087 ± 0.03
B		49.0	50.31	246.8	$1.88^{+0.52}_{-0.31}$	0.084 ± 0.05
C		42.2	43.53	328.0	$2.27^{+1.4}_{-0.6}$	0.096 ± 0.07
D		72.8	73.54	252.6	$2.04^{+0.55}_{-0.34}$	0.151 ± 0.2
E		70.2	71.03	297.2	$2.99^{+7.0}_{-1.2}$	0.010 ± 0.03
F		-30.6	-31.78	286.0	$1.37^{+0.17}_{-0.12}$	0.046 ± 0.003
BS1		25.6	26.65	129.2	$0.39^{+0.01}_{-0.01}$	0.410 ± 0.3
BS2		29.0	30.14	207.0	$1.03^{+0.05}_{-0.05}$	0.210 ± 0.06

NOTES: BS1 and BS2 parameters are from Sromovsky et al. (2012) and represent the brightest parts of the features. PID is the ID for pressure estimation. TID is the tracking ID where applicable. Other headings are as given in Table 3.

at northern middle latitude are found to be well above the methane condensation level and thus likely contain a component of methane ice. Very few of the cloud features have significant optical depths. Even the brightest feature (BS1) has less than one optical depth. A more detailed study of the high-latitude features will require improvements in the S/N of the Hcont images.

8. SUMMARY AND CONCLUSIONS

Following the 2007 equinox, new circulation measurements were obtained from imaging observations by HST in 2009, by Keck in July 2011, and by Gemini-North in October 2011. The new imaging programs used repeated short exposures followed by averaging in latitude-longitude projections to increase signal to noise ratios so that low contrast cloud features could be detected and tracked. Application of high S/N imaging and analysis techniques (Fry et al. 2012) to 2011 observations of Uranus using Gemini and Keck telescopes resulted in detection of many trackable cloud features even under less than ideal observing conditions (for Keck) and less than ideal AO references (for Gemini). The 2011 observations, which provide better views of Uranus' north polar region, have enabled more accurate measurements of the zonal winds at high latitudes. Using 2011 Keck images in July and Gemini images in October, we made measurements of cloud motions using a variety of methods, using manual tracking and guided correlation tracking, as well as

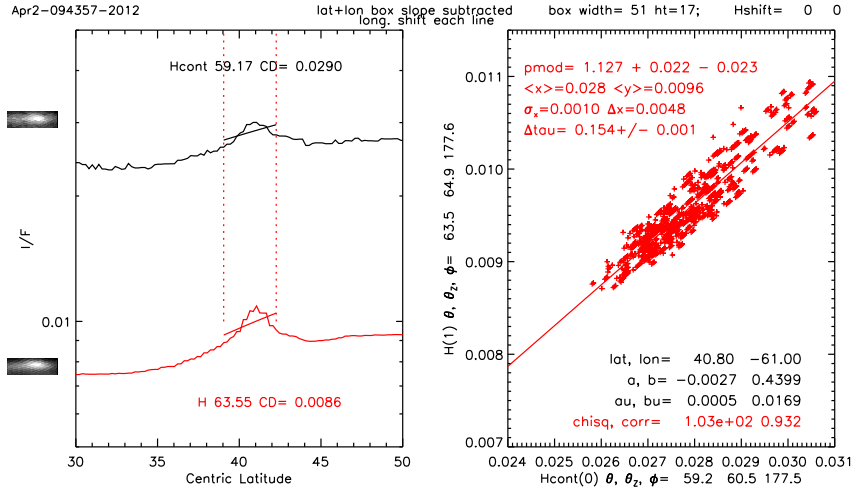


FIG. 19.— I/F vs latitude (left) for H and H_{cont} through target box 3 (in Fig. 18) and correlation plot of I/F observations within that target box (right), with linear regression fit line and inferred pressure (p_{mod}) in bars and optical depth ($\Delta\tau$).

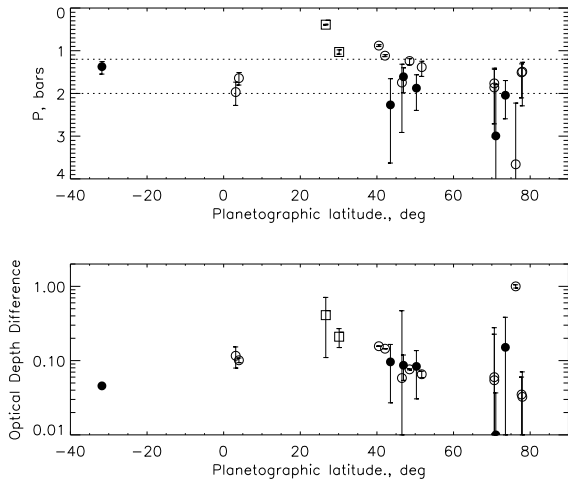


FIG. 20.— Discrete cloud pressure (top) and optical depth perturbation (bottom) inferred from the ratio and amplitude of spatial modulations in H and H_{cont} images. Open circles are from Keck NIRC2 images taken on 26 July 2011, filled circles from Gemini NIRC2 images taken on 26 October 2011, and squares are from Sromovsky et al. (2012).

using high-pass filtered images to enhance small discrete features and median differenced images to enhance larger discrete features, which often appear at low latitudes. Our main conclusions are as follows:

1. Zonal winds measured in 2009 and 2011 are roughly consistent with the 10-term Legendre polynomial fit to 2007 observations (Sromovsky et al. 2009), but deviate in a direction that provides somewhat better agreement with the profile reflected about the equator, which is in the direction of reducing hemispheric asymmetry, although this is not yet statistically significant.
2. The best high latitude results were obtained from Keck 2011 imagery, and clearly define a prograde jet peak near 260 m/s at a planetographic latitude near 60°N.
3. Cloud motions in the north polar region, from the jet peak northward, appear most consistent with

solid body rotation at a rate of 4.3°/h westward relative to the interior. The Voyager wind measurement at 71°S (the only south polar measurement) is consistent with the same rotation period.

4. Using manually guided correlation measurements, we obtained several high accuracy measurements of near equatorial (between 2 and 3° N) drift rates averaging $0.52 \pm 0.02^\circ/\text{h}$ eastward in 2011; this corresponds to a retrograde wind speed of 64 ± 2 m/s, which is in close agreement with new measurements in 2003 Keck images obtained by Hammel et al. (2005).
5. The near-equatorial features (2-4° N) are broad and diffuse, and form a pattern consistent with a wavenumber of 9 (40° spacing in longitude), suggesting that the measured motions might differ from the mean mass flow. The 2011 pattern is not complete, however, and thus the Hammel et al. (2005) wavenumber 12 pattern (also incomplete but better constrained) might be consistent with our results.
6. When 2011 observations are combined with 2009 HST wind results of Fry et al. (2012), the resulting fits provide less asymmetry at high latitudes than found by Sromovsky et al. (2009), mainly because of better constraints obtained from high-latitude measurements. For this data set, the difference in fit quality between symmetric and asymmetric fits is statistically insignificant.
7. When combined with past observations from 1997 onward, which provides better sampling at southern mid latitudes, we find a small but well defined asymmetry at middle latitudes, extending from about 15° to 40°. Longitudinal drift rates at 35° N differ from drift rates at 35° S by an average of 0.2°/h eastward, which corresponds to a wind speed difference of 20 m/s. There is no substantial evidence regarding symmetry properties at high latitudes, primarily due to a lack of samples in the southern hemisphere.

8. Voyager 1986 wind measurements do not differ significantly from the zonal wind profile established by 1997-2011 observations, raising the possibility that the asymmetry at the most recent equinox is a long-term feature of Uranus' circulation, or that the asymmetry has a phase shift relative to seasonal forcing that is less than 90° , or that the asymmetry response function is itself asymmetric, with perhaps most of the asymmetry reversal occurring early in the seasonal cycle. These possibilities can be distinguished by measurements between now and the next solstice in 2030.
9. High accuracy wind measurements at nearby latitudes often differ by far more than their estimated uncertainties, which might be a result of different atmospheric depths, latitude differences between the generating circulation feature and the observed cloud feature, and possible long-period eddy motions.
10. The morphology of cloud features in the north polar region in 2011 is very different from the south polar region observed in 2003. Although the south polar region was devoid of discrete cloud features, the north polar region (north of 60°N) contains small bright (but low contrast cloud features), widely distributed and reminiscent of fair-weather cumulus cloud fields on earth, though on a much larger scale, with features approximately 450 km in size, and spaced roughly 1500-3000 km apart. This morphology, which resembles Saturn's polar regions, is distinct from lower latitudes, where the predominant morphology consists of zonal bands with longitudinally stretched streaky cloud features, and not widely distributed.
11. The north polar region was also found to have small dark spots comparable in size to the small bright features, but considerably less numerous.
12. Where S/N ratios permitted measurement we determined that high latitude bright cloud features were located at pressures at 1.5 bars or deeper, with the most accurate estimates between 1.4 and 2 bars, which is within the main background cloud layer observed on Uranus.
13. Cloud pressures inferred from spatial modulations

in H and Hcont images near the equator were between 1.5 and 2 bars, as were many clouds at northern mid latitudes.

14. A few of the brighter cloud features were found to be close to or above the methane condensation level, the highest being the BS1 feature described by Sromovsky et al. (2012), which reached an estimated pressure near 400 mb.

The cloud pressure and optical depth estimates could be improved in several ways. The first is to compute model ratios for background models that vary in latitude as needed to reproduce the background I/F, instead of using the mid-latitude calculations. The second, which applies to the existing observations, is to determine a more accurate relative measurement of the central disk I/F of Uranus in H and Hcont spectral filters, then apply that calibration to the existing observations. A third improvement could be obtained by improving the S/N ratio of the Hcont measurement, which will require new measurements.

The high S/N methods applied to Keck imaging observations will likely yield even better results with better seeing conditions and a well adjusted AO system. According to the test case of Fry et al. (2012), there is a great potential for further significant improvements in coverage of the zonal wind profile.

ACKNOWLEDGMENTS

We thank Eric Karkoschka and an anonymous reviewer for detailed and constructive suggestions for improving the paper. LAS and PMF acknowledge support from NASA Planetary Astronomy Grant NNX08A051G and Space Telescope Science Institute Grants HST-GO-11639.04-A and HST-GO-12463.05-A. HBH acknowledges support by Grants from NASA's Planetary Astronomy and Atmospheres Programs. IdP acknowledges support from NASA Grant NNX07AK70G. KAR acknowledges support by grants from the Space Telescope Science Institute. This research was partly based on Hubble Space Telescope observations. We thank staff at the W. M. Keck Observatory, which is made possible by the generous financial support of the W. M. Keck Foundation. We thank those of Hawaiian ancestry on whose sacred mountain we are privileged to be guests. Without their generous hospitality none of our groundbased observations would have been possible.

REFERENCES

- de Pater, I., Marchis, F., Macintosh, B. A., Roe, H. G., Le Mignant, D., Graham, J. R., Davies, A. G., 2004. Keck AO observations of Io in and out of eclipse. *Icarus* 169, 250–263.
- de Pater, I., Sromovsky, L., Hammel, H. B., Fry, P. M., LeBeau, R. P., Rages, K. A., Showalter, M. R., Matthews, K., 2011. Post-equinox Observations of Uranus: Berg's Evolution, Vertical Structure, and Track towards the Equator. *Icarus* 215, 332–345.
- Friedson, J., Ingersoll, A. P., 1987. Seasonal meridional energy balance and thermal structure of the atmosphere of Uranus - A radiative-convective-dynamical model. *Icarus* 69, 135–156.
- Fry, P. M., Sromovsky, L. A., de Pater, I., Hammel, H. B., Rages, K. A., 2012. Detection and Tracking of Subtle Cloud Features on Uranus. *Astron. J.* 143, 150–161.
- Hammel, H. B., de Pater, I., Gibbard, S., Lockwood, G. W., Rages, K., 2005. Uranus in 2003: Zonal winds, banded structure, and discrete features. *Icarus* 175, 534–545.
- Hammel, H. B., Lockwood, G. W., 2007. Long-term atmospheric variability on Uranus and Neptune. *Icarus* 186, 291–301.
- Hammel, H. B., Rages, K., Lockwood, G. W., Karkoschka, E., de Pater, I., 2001. New Measurements of the Winds of Uranus. *Icarus* 153, 229–235.
- Hammel, H. B., Sromovsky, L. A., Fry, P. M., Rages, K., Showalter, M., de Pater, I., van Dam, M. A., Lebeau, R. P., Deng, X., 2009. The Dark Spot in the atmosphere of Uranus in 2006: Discovery, description, and dynamical simulations. *Icarus* 201, 257–271.

- Hofstadter, M. D., Butler, B. J., Hammel, H. B., Klein, M. J., 2004. The Discovery of Radio-Bright Northern Latitudes on Uranus: Implications for Weather and Climate. *Bull. Am. Astron. Soc.* 36, 1074.
- Karkoschka, E., 1998. Clouds of High Contrast on Uranus. *Science* 280, 570–572.
- Karkoschka, E., Tomasko, M., 2009. The haze and methane distributions on Uranus from HST-STIS spectroscopy. *Icarus* 202, 287–309.
- Lindal, G. F., Lyons, J. R., Sweetnam, D. N., Eshleman, V. R., Hinson, D. P., 1987. The atmosphere of Uranus - Results of radio occultation measurements with Voyager 2. *J. Geophys. Res.* 92, 14987–15001.
- Rages, K. A., Hammel, H. B., Friedson, A. J., 2004. Evidence for temporal change at Uranus' south pole. *Icarus* 172, 548–554.
- Seidelmann, P. K., Abalakin, V. K., Bursa, M., Davies, M. E., de Bergh, C., Lieske, J. H., Oberst, J., Simon, J. L., Standish, E. M., 2002. Report of the IAU/IAG Working Group on Cartographic Coordinates and Rotational Elements of the Planets and Satellites. *Celestial Mechanics and Dynamical Astronomy* 82, 83–110.
- Showman, A. P., de Pater, I., 2005. Dynamical implications of Jupiter's tropospheric ammonia abundance. *Icarus* 174, 192–204.
- Smith, B. A., Soderblom, L. A., Beebe, R., Bliss, D., Brown, R. H., Collins, S. A., Boyce, J. M., Briggs, G. A., Brahic, A., Cuzzi, J. N., Morrison, D., co-authors, 1986. Voyager 2 in the Uranian system - Imaging science results. *Science* 233, 43–64.
- Sromovsky, L. A., Fry, P. M., 2005. Dynamics of cloud features on Uranus. *Icarus* 179, 459–484.
- Sromovsky, L. A., Fry, P. M., 2007. Spatially resolved cloud structure on Uranus: Implications of near-IR adaptive optics imaging. *Icarus* 192, 527–557.
- Sromovsky, L. A., Fry, P. M., Hammel, H. B., de Pater, I., Rages, K. A., Showalter, M. R., Merline, W. J., Tamblyn, P., Neyman, C., Margot, J.-L., Fang, J., Colas, F., Dauvergne, J.-L., Gómez-Forrellad, J. M., Hueso, R., Sánchez-Lavega, A., Stallard, T., 2012. Episodic bright and dark spots on Uranus. *Icarus* 220, 6–22.
- Sromovsky, L. A., Fry, P. M., Hammel, H. B., Ahue, W. M., de Pater, I., Rages, K. A., Showalter, M. R., van Dam, M. A., 2009. Uranus at equinox: Cloud morphology and dynamics. *Icarus* 203, 265–286.
- Sromovsky, L. A., Fry, P. M., Hammel, H. B., de Pater, I., Rages, K. A., Showalter, M. R., 2007. Dynamics, Evolution, and Structure of Uranus' Brightest Cloud Feature. *Icarus* 192, 558–575.
- Sromovsky, L. A., Fry, P. M., Kim, J. H., 2011. Methane on Uranus: The case for a compact CH₄ cloud layer at low latitudes and a severe CH₄ depletion at high latitudes based on re-analysis of Voyager occultation measurements and STIS spectroscopy. *Icarus* 215, 292–312.
- Sromovsky, L. A., Limaye, S. S., Fry, P. M., 1993. Dynamics of Neptune's Major Cloud Features. *Icarus* 105, 110–141.
- West, R. A., Baines, K. H., Karkoschka, E., Sánchez-Lavega, A., 2009. Clouds and Aerosols in Saturn's Atmosphere. In: Dougherty, M. K., Esposito, L. W., Krimigis, S. M. (Eds.), *Saturn from Cassini-Huygens*. Springer, pp. 161–179.